

# EVOLUTION OF STELLAR-TO-HALO MASS RATIO AT $z = 0 - 7$ IDENTIFIED BY CLUSTERING ANALYSIS WITH THE HUBBLE LEGACY IMAGING AND EARLY SUBARU/HYPER SUPRIME-CAM SURVEY DATA

YUICHI HARIKANE<sup>1,2</sup>, MASAMI OUCHI<sup>1,3</sup>, YOSHIAKI ONO<sup>1</sup>, SURHUD MORE<sup>3</sup>, SHUN SAITO<sup>3</sup>, YEN-TING LIN<sup>4</sup>, JEAN COUPON<sup>5</sup>, KAZUHIRO SHIMASAKU<sup>6,7</sup>, TAKATOSHI SHIBUYA<sup>1</sup>, PAUL A. PRICE<sup>8</sup>, LIHWAI LIN<sup>4</sup>, BAU-CHING HSIEH<sup>4</sup>, MASAFUMI ISHIGAKI<sup>1,2</sup>, YUTAKA KOMIYAMA<sup>9</sup>, JOHN SILVERMAN<sup>3</sup>, TADAFUMI TAKATA<sup>9</sup>, HIROKO TAMAZAWA<sup>1,2</sup>, AND JUN TOSHIKAWA<sup>9</sup>

*Submitted to ApJ*

## ABSTRACT

We present clustering analysis results from 10,540 Lyman break galaxies (LBGs) at  $z \sim 4 - 7$  that are identified in a combination of the Hubble legacy deep imaging and the complimentary large-area Subaru/Hyper Suprime-Cam data taken very recently. We measure angular correlation functions of these LBGs at  $z \sim 4, 5, 6$ , and  $7$ , and fit these measurements using halo occupation distribution (HOD) models that provide the estimates of halo masses,  $M_h \sim (1 - 20) \times 10^{11} M_\odot$ . Our  $M_h$  estimates agree with those obtained by previous clustering studies in a UV-magnitude vs.  $M_h$  plane, and allow us to calculate stellar-to-halo mass ratios (SHMRs) of the LBGs. By comparison with the  $z \sim 0$  SHMR given by SDSS, we identify evolution of the SHMR from  $z \sim 0$  to  $z \sim 4$ , and  $z \sim 4$  to  $z \sim 7$  at the  $> 98\%$  confidence levels. The SHMR decreases by a factor of  $\sim 3$  from  $z \sim 0$  to  $4$ , and increase by a factor of  $\sim 5$  from  $z \sim 4$  to  $7$ . We obtain the baryon conversion efficiency (BCE) of our LBGs at  $z \sim 4$ , and find that the BCE increases with increasing dark matter halo mass. We finally compare our clustering+HOD estimates with the abundance matching results, and conclude that the  $M_h$  estimates of the clustering+HOD analyses agree with those of the simple abundance matching within a factor of 3, and that the agreement is better with those of the sophisticated abundance matching techniques that include subhalos, incompleteness, and/or star formation rate+stellar mass function evolution.

*Keywords:* galaxies: formation — galaxies: evolution — galaxies: high-redshift

## 1. INTRODUCTION

Dark matter halos play an important role in galaxy formation and evolution in the framework of Lambda cold dark matter (ΛCDM) structure formation models. These halos regulate gas cooling processes necessary for star formation. Gas cooling is efficient in halos with masses of  $10^{10} - 10^{13} M_\odot$ , where the gas cooling time scale is shorter than the gas infall time scale (Silk & Wyse 1993). In low and high mass haloes, supernova (SN), radiation pressure, and active galactic nucleus (AGN) feedback are thought to suppress star formation by thermal and kinetic energy inputs (e.g., Murray et al. 2005; Dekel et al. 2009; Kereš et al. 2009; Harikane et al. 2014).

The galaxy-dark matter connection is essential for understanding galaxy formation, and specifically a stellar-to-halo mass ratio (SHMR), which is defined as the ratio of a galaxy's stellar mass to its halo mass, is one of the key quantities. The SHMR indicates the integrated efficiency of the past stellar mass assembly (i.e., star formation and mergers). The SHMR has been theoretically investigated with the help of hydrodynamic simulations or semi-analytic models (e.g., Birrer et al. 2014; Okamoto et al. 2014; Mitchell et al. 2015). In observational studies, the SHMR is measured by galaxy clustering, weak lensing analyses, and satellite kinematics at low-redshift (e.g., Mandelbaum et al. 2006; More et al. 2011; Leauthaud et al. 2012; Hudson et al. 2015; Shan et al. 2015; Rodríguez-Puebla et al. 2015; Coupon et al. 2015; Skibba et al. 2015). These low-redshift studies find that the SHMR has a peak at a dark matter halo mass of  $M_h \sim 10^{12} M_\odot$ , independent of redshift, which is referred to as a pivot halo mass. Leauthaud et al. (2012) claim a redshift evolution of SHMRs (and pivot halo masses) from  $z \sim 0$  to  $z \sim 1$ . Although some studies estimate SHMR by utilizing clustering analysis at redshift beyond 1 (e.g., Foucaud et al. 2010; Durkalec et al. 2015; McCracken et al. 2015; Hatfield et al. 2015), it is difficult to investigate the evolution of SHMR at  $z > 1$  due to the poor statistics from small galaxy samples available to date (c.f., McCracken et al. 2015; Hatfield et al. 2015).

The abundance matching technique is another indirect probe of the SHMR. The abundance matching technique connects galaxies to their host dark matter haloes by matching the cumulative stellar mass function (or the cumulative luminosity function) and the cumulative halo mass function. Because the abundance match-

<sup>1</sup> Institute for Cosmic Ray Research, The University of Tokyo, 5-1-5 Kashiwanoha, Kashiwa, Chiba 277-8582, Japan

<sup>2</sup> Department of Physics, Graduate School of Science, The University of Tokyo, 7-3-1 Hongo, Bunkyo, Tokyo, 113-0033, Japan

<sup>3</sup> Kavli Institute for the Physics and Mathematics of the Universe (Kavli IPMU, WPI), University of Tokyo, Kashiwa, Chiba 277-8583, Japan

<sup>4</sup> Institute of Astronomy & Astrophysics, Academia Sinica, Taipei 106, Taiwan (R.O.C.)

<sup>5</sup> Astronomical Observatory of the University of Geneva, ch. d'Ecogia 16, 1290 Versoix, Switzerland

<sup>6</sup> Department of Astronomy, Graduate School of Science, The University of Tokyo, Hongo, Bunkyo, Tokyo 113-0033, Japan

<sup>7</sup> Research Center for the Early Universe, The University of Tokyo, Hongo, Tokyo 113-0033, Japan

<sup>8</sup> Princeton University Observatory, Peyton Hall, Princeton, NJ 08544, USA

<sup>9</sup> National Astronomical Observatory, Mitaka, Tokyo 181-8588, Japan

<sup>10</sup> Center for Astronomy and Astrophysics, Department of Physics & Astronomy, Shanghai Jiao Tong University, 800 Dongchuan Road, Shanghai, 200240, China

ing technique only requires one-point statistics that are easily measured, many recent studies apply the abundance matching technique from low-redshift to high-redshift galaxies (Moster et al. 2013; Behroozi et al. 2013a; Finkelstein et al. 2015; Mashian et al. 2015; Trac et al. 2015; Saito et al. 2015). Behroozi et al. (2013a) investigate the SHMR by the abundance matching technique using stellar mass functions as well as specific star formation rates and cosmic star formation rates, and find that the SHMR evolves from  $z = 0$  to  $z = 8$ . Although the abundance matching technique is a useful and less expensive method to connect galaxies to their dark matter haloes, there are two major systematic uncertainties for high-redshift galaxies. One uncertainty is the star-formation duty cycle (DC), which is defined as the probability of a halo of given mass to host an observable star forming galaxy. Most abundance matching studies for  $z \gtrsim 4$  Lyman break galaxies (LBGs) use UV luminosity functions, assuming their star-formation (i.e. UV-bright phase) DC is unity (c.f., Behroozi et al. 2013a). However, the star formation activity should be episodic. Moreover, unknown populations of passive and dusty star-forming galaxies are expected to exist. In fact, Lee et al. (2009) claim that the DC is  $\sim 0.3$  at  $z \sim 4$ , and Ouchi et al. (2001) indicate a halo mass-dependent DC based on the clustering analysis. The other uncertainty is the subhalo-galaxy relation. Although a majority of abundance matching studies include subhalos (subhalo abundance matching; e.g., Moster et al. 2013; Behroozi et al. 2013a; Finkelstein et al. 2015; Mashian et al. 2015), the subhalo-galaxy relation is highly unknown. For example, which subhalo property best correlates with the stellar mass (or luminosity) is still under discussion (Reddick et al. 2013; Guo et al. 2015). Thus, one needs information independent from abundance to understand these systematics. Because the lensing analysis is not feasible for galaxies at  $z \gtrsim 2$  due to the limited background source numbers and image qualities, clustering analysis is a promising technique to test the abundance matching results and to extend the studies of the galaxy-dark matter connection.

A wide-field mosaic CCD camera, Hyper Suprime-Cam (HSC; Miyazaki et al. 2012), has been installed at the prime focus of the Subaru telescope. HSC has a field-of-view (FoV) of  $1.75 \text{ deg}^2$  with a high sensitivity accomplished with the Subaru 8m primary mirror. An HSC legacy survey under the Subaru Strategic Program (SSP; PI: S. Miyazaki) has been allocated 300 nights in 5 years, and has started since March 2014.<sup>11</sup> The HSC SSP has three survey layers of Wide, Deep, and Ultradeep that will cover the sky areas of  $1400$ ,  $27$ , and  $3.5 \text{ deg}^2$  with the  $5\sigma$  point-source limiting magnitudes of  $r \simeq 26 \text{ mag}$ ,  $r \simeq 27 \text{ mag}$ , and  $r \simeq 28 \text{ mag}$ , respectively. It is expected that full HSC SSP data sets will provide us with  $\sim 2 \times 10^7$  LBGs at  $z \gtrsim 4$ , which are  $\sim 400$  times larger than those found in the deep fields of the Canada-France-Hawaii Telescope Legacy Survey (CFHTLS; Hildebrandt et al. 2009) and allow us to investigate statistical properties of LBGs down to  $\sim 0.1L^*$ . Complementing these HSC SSP efforts, recent deep Hubble Space Telescope observations with Advanced Camera for Surveys (ACS)

and Wide Field Camera 3 (WFC3) provide samples of  $> 10^4$  LBGs whose luminosities reach below  $\sim 0.1L^*$  (e.g., Bouwens et al. 2015; Ishigaki et al. 2015). In this study, we use the unique data sets of Subaru/HSC and Hubble/ACS+WFC3 to investigate the galaxy-dark matter connection with LBGs in a wide luminosity range, and investigate SHMRs at  $z \gtrsim 4$ , for the first time, using clustering analyses.

This paper is organized as follows. We present the observational data sets of Subaru/HSC and Hubble/ACS+WFC3 in Section 2. We show the photometry and the sample selection of LBGs in Section 3. Our clustering analyses are presented in Section 4. Sections 5 and 6 detail our results of the dark matter halo mass and SHMR, respectively. We discuss implications of the SHMR evolution and differences between our results and abundance matching results in Section 7. Section 8 summarizes our findings. Throughout this paper we use the following cosmological model:  $\Omega_m = 0.3$ ,  $\Omega_\Lambda = 0.7$ ,  $\Omega_b = 0.045$ ,  $H_0 = 70 \text{ km s}^{-1} \text{ Mpc}^{-1}$ , and  $\sigma_8 = 0.8$ . We use  $r_{200}$  that is the radius in which the mean enclosed density is 200 times higher than the mean cosmic density. To define the halo mass, we use  $M_{200}$  that is the total mass enclosed in  $r_{200}$ . We assume a Chabrier (2003) initial mass function (IMF). All magnitudes are in the AB system.

## 2. OBSERVATIONAL DATA SETS

### 2.1. Hubble Data

We use 10 deep optical-NIR imaging data sets of Hubble Ultra Deep Field (HUDF), Great Observatories Origins Deep Survey (GOODS)-North-Deep, GOODS-North-Wide, GOODS-South-Deep, GOODS-South-Wide, Cosmic Assembly Near-infrared Deep Extragalactic Legacy Survey (CANDELS)-All-Wavelength Extended Groth Strip International Survey (AEGIS), CANDELS-Cosmological Evolution Survey (COSMOS), CANDELS-Ultra Deep Survey (UDS), Hubble Frontier Field (HFF)-Abell2744P, and HFF-MACS0416P that are taken with ACS and WFC3 on the Hubble Space Telescope. The total area of the Hubble data we use is  $\sim 600 \text{ arcmin}^2$ . We mask image regions that are contaminated by halos of bright stars or diffraction spikes by visual inspection, and measure limiting magnitudes in a  $0''.35$ -diameter circular aperture with SDFRED (Yagi et al. 2002; Ouchi et al. 2004a), after homogenizations of point-spread functions (PSFs; see Section 3.1.1 for more details). The typical FWHMs of the PSFs of ACS and WFC3 images are  $0''.1$  and  $0''.2$ , respectively. The limiting magnitudes, PSF FWHMs, and effective areas of these images are summarized in Table 1.

#### 2.1.1. HUDF

HUDF has the deepest ACS and WFC3 imaging data, ever taken, from the combination of the three surveys, HUDF (Beckwith et al. 2006), HUDF09 (GO 11563; PI: G. Illingworth; e.g., Bouwens et al. 2010), and HUDF12 (GO 12498; PI: R. Ellis; e.g., Ellis et al. 2013; Koekoemoer et al. 2013). We use the combined HUDF data set compiled by the eXtreme Deep Field (XDF) team<sup>12</sup> (Illingworth et al. 2013). The HUDF data consist of 9-band images of  $B_{435}V_{606}i_{775}I_{814}z_{850}Y_{105}J_{125}JH_{140}H_{160}$ ,

<sup>11</sup> <http://www.naoj.org/Projects/HSC/surveyplan.html>

<sup>12</sup> <https://archive.stsci.edu/prepds/xdx/>

**Table 1**  
Limiting Magnitudes of the Hubble Data

Field (1)	Area (arcmin <sup>2</sup> ) (2)	5 $\sigma$ Limiting Magnitude Hubble										CFHT/Subaru $r$ (13)
		$B_{435}$ (3)	$V_{606}$ (4)	$i_{775}$ (5)	$I_{814}$ (6)	$z_{850}$ (7)	$Y_{105}$ (8)	$J_{125}$ (9)	$JH_{140}$ (10)	$H_{160}$ (11)	coadd <sup>a</sup> (12)	
HUDF	3.7	30.0	30.5	30.1	29.3	29.6	30.2	29.9	29.8	29.9	30.6	...
GOODS-N-Deep	57.4	28.6	28.8	28.3	30.5	28.1	27.9	28.3	...	28.1	28.6	...
GOODS-N-Wide	58.2	28.6	28.7	28.2	29.9	28.0	27.7	27.6	...	27.5	28.1	...
GOODS-S-Deep	52.1	28.6	28.8	28.2	28.8	29.0	28.4	28.4	...	28.3	29.0	...
GOODS-S-Wide	30.4	28.6	28.8	28.2	28.4	28.0	27.7	27.8	...	27.6	28.3	...
CANDELS-AEGIS	174.9	...	28.3	27.8	...	...	...	27.6	...	27.7	28.0	28.1
CANDELS-COSMOS	122.0	...	28.3	28.0	...	...	...	27.6	...	27.6	27.9	27.9/27.7
CANDELS-UDS	129.3	...	28.2	28.2	...	...	...	27.5	...	27.6	27.9	28.2
HFF-Abell2744P	3.1	28.8	29.1	...	28.8	...	29.0	28.8	28.8	28.8	29.3	...
HFF-MACS0416P	3.8	28.6	28.9	...	28.8	...	29.3	29.1	29.1	29.0	29.5	...
PSF FWHM <sup>b</sup>		0''.12	0''.11	0''.10	0''.11	0''.21	0''.20	0''.20	0''.20	0''.20	0''.21	0''.8

**Note.** — Columns: (1) Field. (2) Effective Area in arcmin<sup>2</sup>. (3)–(12) Limiting magnitudes which correspond to 5 $\sigma$  variations in the sky flux measured in a circular aperture of 0''.35-diameter in PSF-matched images. (13) Limiting magnitude defined by a 5 $\sigma$  sky noise in a 1''.0-diameter aperture. See Skelton et al. (2014) for limiting magnitudes in other bands.

<sup>a</sup> Coadd image of  $Y_{105}J_{125}JH_{140}H_{160}$ -bands.

<sup>b</sup> Mean PSF FWHM values.

and cover  $\sim 4$  arcmin<sup>2</sup> sky area. The 5 $\sigma$  limiting magnitudes are  $\sim 30$  mag over these 9 bands.

#### 2.1.2. GOODS-North and GOODS-South

We use the data sets of GOODS-North and GOODS-South fields, available on the CANDELS and 3D-HST (Brammer et al. 2012; Skelton et al. 2014) websites,<sup>13</sup> that are obtained by CANDELS (PIs: S. Faber and H. Ferguson; Grogin et al. 2011; Koekemoer et al. 2011). The GOODS fields are composed of deep and wide survey data whose 5 $\sigma$  limiting magnitudes are typically  $\sim 28.5$  mag and  $\sim 27.5$  mag, respectively. About half of the GOODS-North and GOODS-South fields are deep survey areas, and the remaining half of the GOODS-North and quarter of the GOODS-South fields are wide survey areas. The GOODS-North and GOODS-South data are observed with bands of  $B_{435}V_{606}i_{775}I_{814}z_{850}Y_{105}J_{125}H_{160}$  in effective areas of  $\sim 120$  and  $\sim 90$  arcmin<sup>2</sup>, respectively.

#### 2.1.3. CANDELS-AEGIS, CANDELS-COSMOS, and CANDELS-UDS

The largest-area Hubble data sets in our study come from CANDELS-AEGIS, CANDELS-COSMOS, and CANDELS-UDS imaging data (Grogin et al. 2011; Koekemoer et al. 2011) available at the 3D-HST website (Brammer et al. 2012; Skelton et al. 2014). These imaging regions are covered by the ACS  $V_{606}I_{814}$  and WFC3  $J_{125}H_{160}$  observations with the typical 5 $\sigma$  limiting magnitude of 27.5 mag. Ground-based optical images taken with the CFHT and Subaru telescope are also available for these fields. We use the CFHT  $ugr$  band images in the CANDELS-AEGIS field, the CFHT  $ugr$  and Subaru  $BVr$  band images in the CANDELS-COSMOS field, and the CFHT  $u$  and Subaru  $BVr$  band images in the CANDELS-UDS field, all of which are available on the 3D-HST website.

#### 2.1.4. HFF-Pallares

Our study also includes imaging data from HFF (PI J. Lotz; e.g., Ishigaki et al. 2015; Kawamata et al. 2015). These data are parallel-field observation images of Abell2744 and MACS0416 galaxy clusters that are taken from the HFF website.<sup>15</sup> Because the lensing effects such as magnification and survey volume distortion are negligibly weak in HFF parallel fields (see, e.g., Ishigaki et al. 2015), we regard these HFF parallel images as blank field data. These two HFF parallel fields are observed with 7 bands of  $B_{435}V_{606}I_{814}Y_{105}J_{125}JH_{140}H_{160}$  over a total effective area of  $\sim 7$  arcmin<sup>2</sup>. The typical 5 $\sigma$  limiting magnitude is 29.0 mag.

#### 2.2. Subaru Data

Our study includes early data of the HSC SSP survey taken from March to November in 2014 (S14A\_0b). We use the HSC SSP Wide layer *griz* data of the XMM field (R.A. = 2<sup>h</sup>17<sup>m</sup>00<sup>s</sup>, decl. =  $-5^{\circ}12'00''$  [J2000]) and GAMA09h field (R.A. = 8<sup>h</sup>47<sup>m</sup>00<sup>s</sup>, decl. =  $0^{\circ}45'00''$  [J2000]).<sup>16</sup> Although the HSC data is  $\sim 3 - 6$  magnitude shallower than the Hubble data, the HSC data cover  $\sim 90$  times larger effective area: 8.3 and 6.9 deg<sup>2</sup>, in XMM and GAMA09h, respectively. Thus, the HSC data can provide clustering measurements at the bright end. These HSC data are reduced by the HSC SSP collaboration with hscPipe (version 3.4.1) that is the HSC data reduction pipeline based on the Large Synoptic Survey Telescope (LSST) software pipeline (Ivezic et al. 2008; Axelrod et al. 2010). The HSC data reduction pipeline performs CCD-by-CCD reduction+calibration for astrometry, warping, coadding, and photometric zeropoint measurements. The astrometric and photometric calibration are based on the data of Panoramic Survey Telescope and Rapid Response System (Pan-STARRS) 1 imaging survey (Magnier et al. 2013; Schlafly et al. 2012; Tonry et al. 2012). We mask imaging regions contaminated with diffraction spikes and halos of bright stars using the mask extension outputs from the HSC data reduction

<sup>13</sup> <http://candels.ucolick.org/>

<sup>14</sup> <http://3dhst.research.yale.edu/Home.html>

<sup>15</sup> <http://www.stsci.edu/hst/campaigns/frontier-fields/>

<sup>16</sup> These are the central coordinates of the early HSC data that we use.

**Table 2**  
Limiting Magnitudes of the Subaru/HSC Data

Field (1)	Area (arcmin <sup>2</sup> ) (2)	5 $\sigma$ Limiting Magnitude			
		<i>g</i> (3)	<i>r</i> (4)	<i>i</i> (5)	<i>z</i> (6)
HSC-XMM	30100	26.3	25.8	25.8	25.1
HSC-GAMA09h	24800	26.3	25.7	25.3	25.0
PSF FWHM <sup>a</sup>		0''.82	0''.85	0''.62	0''.67

**Note.** — Columns: (1) Field. (2) Effective Area in arcmin<sup>2</sup>. (3)-(6) Limiting magnitudes defined by a 5 $\sigma$  sky noise in a PSF-75%-flux-radius circular aperture in PSF-matched images.

<sup>a</sup> Mean PSF FWHM values.

pipeline and information of bright stars from our source catalogs (Section 3.2.1) and the Sloan Digital Sky Survey (SDSS) DR12 (Alam et al. 2015).<sup>17</sup> We use the PSF outputs from the pipeline (Jee & Tyson 2011), and typical PSF FWHMs are 0''.6–0''.9. The 5 $\sigma$  limiting magnitudes measured with SDFRED are  $\sim 25 - 26$  mag (Table 2).

### 3. PHOTOMETRIC SAMPLES AND LBG SELECTIONS

#### 3.1. Hubble Samples

##### 3.1.1. Multi-band Photometric Catalogs

We make multi-band source catalogs from the Hubble data. To measure object colors, we match the image PSFs to the WFC3  $H_{160}$ -band images whose typical FWHM of the PSF is  $\simeq 0''.2$ , the largest among the Hubble multi-band images. We utilize SWARP (Bertin et al. 2002), and make our detection images that are co-added data of  $Y_{105}$ ,  $J_{125}$ ,  $JH_{140}$  and  $H_{160}$ -band images. The 5 $\sigma$  limiting magnitudes of the detection images are typically  $\sim 0.5$  mag deeper than those of the single-band images (Table 1).

We perform source detection and photometry for the Hubble images with SExtractor (Bertin & Arnouts 1996). We run SExtractor (version 2.8.6) in dual-image mode for each multi-band image with its detection image, having the parameter set of DETECT\_MINAREA = 6, DETECT\_THRESH = 2.0, ANALYSIS\_THRESH = 2.0, DEBLEND\_NTHRESH = 32, and DEBLEND\_MINCOUNT = 0.005. The total number of the objects identified is 130,655. We measure object colors with MAG\_APER magnitudes defined in a 0''.35-diameter circular aperture. In the CANDELS-AEGIS, CANDELS-COSMOS, and CANDELS-UDS fields, we use the CFHT and Subaru imaging data whose photometry are useful for reducing low- $z$  interlopers from high- $z$  galaxy samples. Because we only need magnitude upper limits of high- $z$  galaxy candidates for this purpose, we do not homogenize the PSFs of CFHT and Subaru images. We obtain aperture magnitudes of SExtractor MAG\_APER with a 1''.0-diameter circular aperture in dual-image mode. If a source is not detected either in a Hubble or CFHT/Subaru band, we replace the source flux with the 1 $\sigma$ -upper limit flux.

##### 3.1.2. Lyman Break Galaxy Selection

We select LBGs from our source catalogs using color information. From the HUDF, GOODS-North, and GOODS-South source catalogs, we select LBGs at  $z \sim 4$ ,

5, 6, and 7 with the following LBG color criteria given in Bouwens et al. (2015):

$z \sim 4$

$$B_{435} - V_{606} > 1, \quad (1)$$

$$i_{775} - J_{125} < 1, \quad (2)$$

$$B_{435} - V_{606} > 1.6(i_{775} - J_{125}) + 1. \quad (3)$$

$z \sim 5$

$$V_{606} - i_{775} > 1.2, \quad (4)$$

$$z_{850} - H_{160} < 1.3, \quad (5)$$

$$V_{606} - i_{775} > 0.8(z_{850} - H_{160}) + 1.2. \quad (6)$$

$z \sim 6$

$$i_{775} - z_{850} > 1.0, \quad (7)$$

$$Y_{105} - H_{160} < 1.0, \quad (8)$$

$$i_{775} - z_{850} > 0.777(Y_{105} - H_{160}) + 1.0. \quad (9)$$

$z \sim 7$

$$z_{850} - Y_{105} > 0.7, \quad (10)$$

$$J_{125} - H_{160} < 0.45, \quad (11)$$

$$z_{850} - Y_{105} > 0.8(J_{125} - H_{160}) + 0.7. \quad (12)$$

We select galaxies that have a Lyman break by the criteria of Equations (1), (4), (7), and (10), and exclude intrinsically-red galaxies by the criteria of Equations (2), (3), (5), (6), (8), (9), (11), and (12). Figure 1 presents these color selection criteria, together with the HUDF catalog sources. These LBG color selection criteria are extensively tested by simulations, and used to study evolution of the UV luminosity functions (e.g., Bouwens et al. 2015).

In the five fields of CANDELS-AEGIS, CANDELS-COSMOS, CANDELS-UDS, HFF-Abell2744P, and HFF-MACS0416P, the available multi-bands are smaller than those in HUDF and GOODS. We use different color criteria, and select LBGs only at  $z \sim 5$ , 6, and 7–8 in these five fields:

$z \sim 5$

$$V_{606} - I_{814} > 1.3, \quad (13)$$

$$I_{814} - H_{160} < 1.25, \quad (14)$$

$$V_{606} - I_{814} > 0.72(I_{814} - H_{160}) + 1.3. \quad (15)$$

$z \sim 6$

$$I_{814} - J_{125} > 0.8, \quad (16)$$

$$J_{125} - H_{160} < 0.4, \quad (17)$$

$$I_{814} - J_{125} > 2(J_{125} - H_{160}) + 0.8. \quad (18)$$

$z \sim 7 - 8$

$$I_{814} - J_{125} > 2.2, \quad (19)$$

$$J_{125} - H_{160} < 0.4, \quad (20)$$

$$I_{814} - J_{125} > 2(J_{125} - H_{160}) + 2.2. \quad (21)$$

We select galaxies that have a Lyman break by the criteria of Equations (13), (16), and (19), and exclude intrinsically-red galaxies by the criteria of Equations (14), (15), (17), (18), (20), and (21).

In addition to these color criteria, we also adopt the following four criteria that are similar to those in Bouwens

<sup>17</sup> <http://www.sdss.org/dr12/>

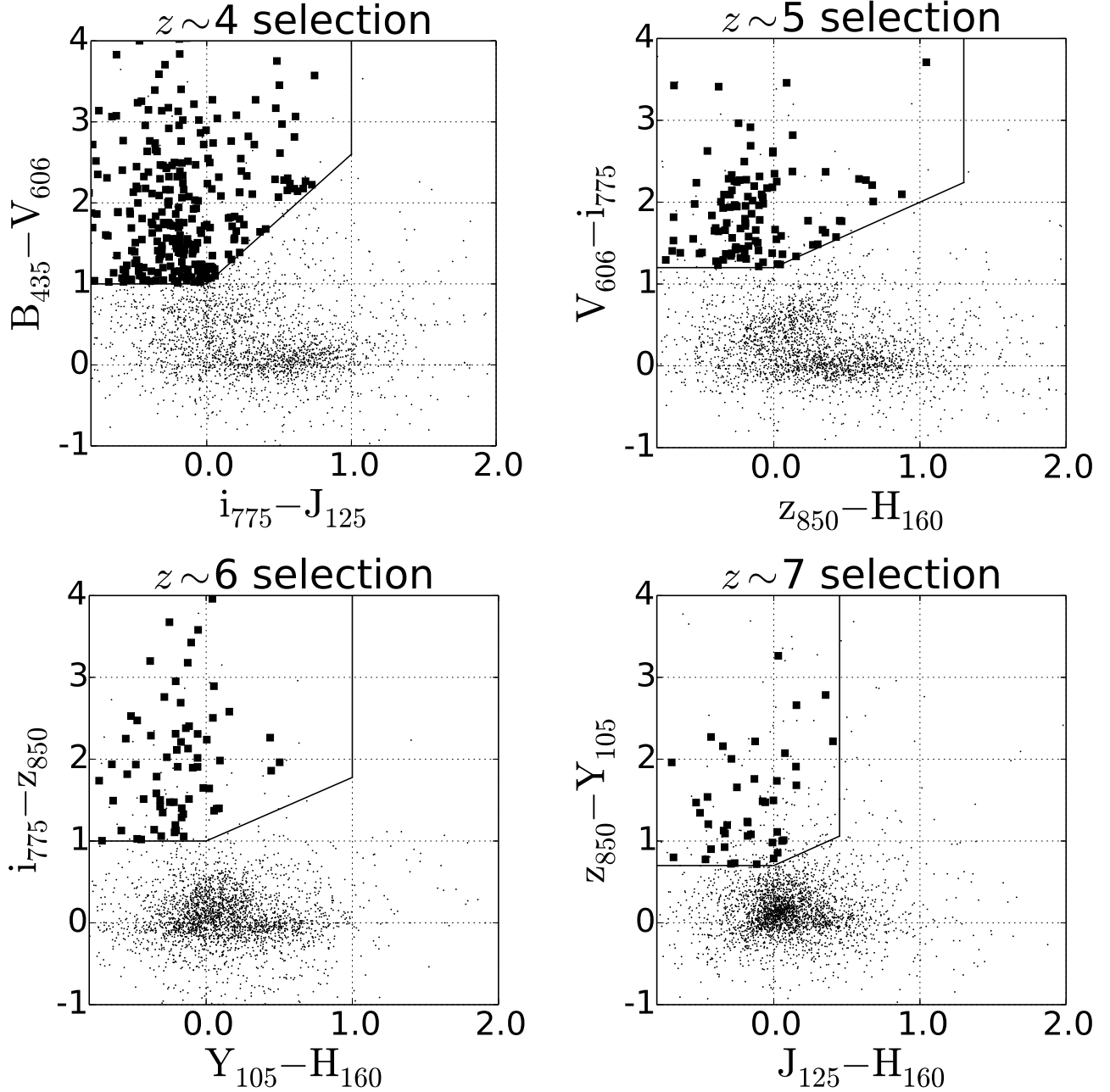


**Figure 1.** Two-color diagrams for selection of LBGs at  $z \sim 4, 5, 6$ , and  $7$  from the Hubble data. The color selection criteria are indicated with solid lines. The black squares and dots denote colors of selected LBGs and other objects in the HUDF region, respectively. In addition to the color criteria indicated by the solid lines, we also enforce other criteria such as a non-detection in the available images blueward of the Lyman break (see Section 3.1.2 for details).

et al. (2015). First, to identify secure sources, we apply detection limits of  $> 5\sigma$  and  $> 5.5\sigma$  levels in the detection images in HUDF and the other fields, respectively. Since HUDF data are deep and clean, the detection criterion of HUDF is moderately loosened than the other fields. Second, for reducing foreground interlopers, we remove sources with a continuum at a wavelength shorter than Lyman breaks of the target LBGs. In all of the Hubble fields except CANDELS-AEGIS, CANDELS-COSMOS, and CANDELS-UDS, we apply the criterion of  $< 2\sigma$  non-detection in  $B_{435}$  band for the candidates of LBGs at  $z \sim 5$  and  $z \sim 6$ , if  $B_{435}$  data are available. Additionally, we require  $< 2\sigma$  non-detection in

$V_{606}$  band or  $V_{606} - z_{850} > 2.6$  for the  $z \sim 6$  LBG candidates. For the  $z \sim 7$  LBG candidates, we calculate an optical  $\chi^2$  value for each source with the  $B_{435}V_{606}i_{775}$  flux measurements, if available, in the same manner as Bouwens et al. (2011). The optical  $\chi^2$  value is defined by  $\chi_{\text{opt}}^2 = \sum_i \text{SGN}(f_i)(f_i/\sigma_i)^2$ , where  $f_i$ ,  $\sigma_i$ , and  $\text{SGN}(f_i)$  are the flux in each band, its uncertainty, and its sign, respectively. We remove  $z \sim 7$  LBG candidates whose  $\chi_{\text{opt}}^2$  values are larger than 4. In the rest of the fields, CANDELS-AEGIS, CANDELS-COSMOS, and CANDELS-UDS, we calculate  $\chi_{\text{opt}}^2$  values with the ground-based band data whose bandpass ranges are shorter than the redshifted

Lyman break wavelength for the target LBGs at  $z \sim 5$ , 6, and 7. We use a threshold value of 2, 3, or 4 that corresponds to the ground-based band numbers of  $< 3$ , 3, or  $> 4$ , respectively (Bouwens et al. 2015), and remove LBG candidates whose  $\chi_{\text{opt}}^2$  value is larger than the threshold. Third, to isolate LBGs from foreground Galactic stars, the LBG candidates should have an SExtractor stellarity parameter, `CLASS_STAR`, less than 0.9 (Hildebrandt et al. 2009; Bouwens et al. 2015), if the candidates are 1 magnitude brighter than the detection limit. Finally, to avoid multiple identifications of a source satisfying two sets of selection criteria for different redshift LBGs, we keep the source in a catalog of LBGs at a redshift higher than the other, and remove the source from the other low- $z$  catalog. For example, if a source meets the criteria of Equations (4)-(6) and (7)-(9), the source is not included in the LBG catalog of  $z \sim 5$ , but  $z \sim 6$ . After adopting these criteria, the estimated contamination fractions by foreground galaxies are estimated to be  $f_c \sim 2$ , 5, 7, and 9% for the  $z \sim 4$ , 5, 6, and 7 LBG samples, respectively, based on the Monte-Carlo simulations in Bouwens et al. (2015).

We thus select a total of 5185, 3694, 978, and 565 LBGs at  $z \sim 4$ , 5, 6, and 7, respectively, from the Hubble data. Table 3 shows magnitudes of the LBGs. For conservative estimates of the clustering signals, we use the LBGs whose magnitudes in the rest-frame UV band,  $m_{\text{UV}}$ , are brighter than the  $5\sigma$  limiting magnitudes. The rest-frame UV band is defined by the available observation band whose central wavelength is nearest to rest-frame 1500 Å for our LBG samples of the Hubble data as well as the Subaru data (Section 3.2). Table 4 summarizes the numbers of LBGs. In Figure 2, we plot the surface number densities of our LBGs, and compare those of LBGs found in the previous study (Bouwens et al. 2015). We confirm that the surface number densities of our LBGs are consistent with those from the previous study. The mean redshifts of the  $z \sim 4$ , 5, 6, and 7 LBGs are  $z_c = 3.8$ , 4.9, 5.9, and 6.8, respectively, and the redshift distributions are the same as those shown in Figures 1 and 19 of Bouwens et al. (2015).

### 3.2. Subaru Samples

#### 3.2.1. Multi-band Photometric Catalogs

We make HSC source catalogs from the reduced images in the same manner as the Hubble source catalogs. First, we homogenize the PSFs of the HSC images to  $\sim 0''.9$  in FWHM by convolving images with a Gaussian, matching a PSF's 75%-flux circular radius that includes 75% of a total flux for a PSF profile source. We then run SExtractor (version 2.8.6) in dual-image mode to detect sources in the detection image, and to carry out photometry in the HSC images for `MAG_APER` in a circular aperture of the PSF's 75%-flux radius. We use the parameter set of `DETECT_MINAREA = 6`, `DETECT_THRESH = 1.5`, `ANALYSIS_THRESH = 1.5`, `DEBLEND_NTHRESH = 32`, and `DEBLEND_MINCOUNT = 0.005`.

#### 3.2.2. Lyman Break Galaxy Selection

We select LBGs at  $z \sim 5$  with the HSC source catalogs, applying color criteria similar to those of the CFHT study (Hildebrandt et al. 2009) that uses the photometric system almost identical to the one of our HSC data.

The  $z \sim 5$  color selection criteria for the HSC sources are

$$r - i > 1.2, \quad (22)$$

$$i - z < 0.7, \quad (23)$$

$$r - i > 1.5(i - z) + 1.0. \quad (24)$$

We select galaxies that have a Lyman break by the criterion of Equation (22), and exclude intrinsically-red galaxies by the criteria of Equations (23) and (24). These LBG color selection criteria are used for the study of clustering evolution (e.g., Hildebrandt et al. 2009).

In addition to the selection criteria above, we require sources to be detected at the  $> 5\sigma$  level in the  $z$ -band image, and to be undetected at the  $< 2\sigma$  level in the  $g$ -band image. We also apply a criterion of SExtractor stellarity parameter, `CLASS_STAR`, of  $< 0.9$ . We thus obtain 730 LBGs at  $z \sim 5$ . The surface number densities of our HSC LBGs are presented in Figure 2, which agree with the previous study results of Hildebrandt et al. (2009). More details of the data reduction and the LBG selection are presented in Y. Ono et al. (in preparation).

## 4. CLUSTERING ANALYSIS

### 4.1. Angular Correlation Function

We derive the angular correlation functions,  $\omega(\theta)$ , with our LBG samples. We calculate observed angular correlation functions,  $\omega_{\text{obs}}(\theta)$ , with the estimator presented in Landy & Szalay (1993),

$$\omega_{\text{obs}}(\theta) = \frac{DD(\theta) - 2DR(\theta) + RR(\theta)}{RR(\theta)}, \quad (25)$$

where  $DD(\theta)$ ,  $DR(\theta)$ , and  $RR(\theta)$  are numbers of galaxy-galaxy, galaxy-random, and random-random pairs normalized by a total number of pairs. We create a random sample composed of 10,000 (100,000) sources for each Hubble (Subaru) field with the geometrical shape same as the observational data including the mask positions. The errors are estimated by the bootstrap technique of Ling et al. (1986) with 100 resamples replacing individual galaxies for each field. It is known that this bootstrap technique tends to overestimate the errors of the correlation function (Fisher et al. 1994; Mo et al. 1992). Although we cannot quantitatively evaluate this trend with our data that are not large enough, the forthcoming data of the HSC survey will enable us to investigate this effect.

Due to the finite size of survey fields, the observed angular correlation function is underestimated by a constant value known as the integral constraint,  $IC$  (Groth & Peebles 1977). Including the correction for the number of objects in the sample,  $N$  (Peebles 1980), the true angular correlation function is given by

$$\omega(\theta) = \omega_{\text{obs}}(\theta) + IC + \frac{1}{N}. \quad (26)$$

We estimate the integral constraint with

$$IC = \frac{\sum_i RR(\theta_i) \omega_{\text{model}}(\theta_i)}{\sum_i RR(\theta_i)}, \quad (27)$$

where  $\omega_{\text{model}}(\theta)$  is the best-fit model angular correlation function, and  $i$  refers the angular bin.

**Table 3**  
Catalog of LBGs in the Hubble Data

Catalog ID	R.A. (J2000)	decl. (J2000)	$B_{435}$	$V_{606}$	$i_{775}$	$I_{814}$	$z_{850}$	$Y_{105}$	$J_{125}$	$JH_{140}$	$H_{160}$	coadd <sup>a</sup>
z4_gdsd_7260	53.074684744	-27.880245679	$29.4 \pm 0.5$	$28.0 \pm 0.1$	$27.7 \pm 0.1$	$27.9 \pm 0.1$	$28.0 \pm 0.1$	$27.8 \pm 0.1$	$28.1 \pm 0.2$	...	$27.6 \pm 0.1$	$28.2 \pm 0.1$
z4_gdsd_7269	53.075142909	-27.880051154	$29.1 \pm 0.4$	$27.6 \pm 0.1$	$27.3 \pm 0.1$	$27.4 \pm 0.1$	$27.3 \pm 0.0$	$27.7 \pm 0.1$	$27.6 \pm 0.1$	...	$27.8 \pm 0.1$	$27.9 \pm 0.1$
z4_gdsd_7328	53.064744909	-27.87986999	$29.4 \pm 0.5$	$27.6 \pm 0.1$	$27.3 \pm 0.1$	$27.3 \pm 0.1$	$27.3 \pm 0.0$	$27.4 \pm 0.1$	$27.4 \pm 0.1$	...	$27.7 \pm 0.1$	$28.6 \pm 0.2$
z4_gdsd_7433	53.065422101	-27.879309789	$< 30.3$	$29.4 \pm 0.4$	$28.2 \pm 0.2$	$28.2 \pm 0.1$	$28.6 \pm 0.2$	$28.5 \pm 0.2$	$28.1 \pm 0.2$	...	$28.0 \pm 0.2$	$28.9 \pm 0.2$
...	...	...	...	...	...	...	...	...	...	...	...	...

**Note.** — All magnitudes listed are measured in  $0''.35$ -diameter circular apertures. Upper limits are  $1\sigma$ .

<sup>a</sup> Coadd image of  $Y_{105}J_{125}JH_{140}H_{160}$ -bands.

(The complete table is available in a machine-readable form in the online journal.)

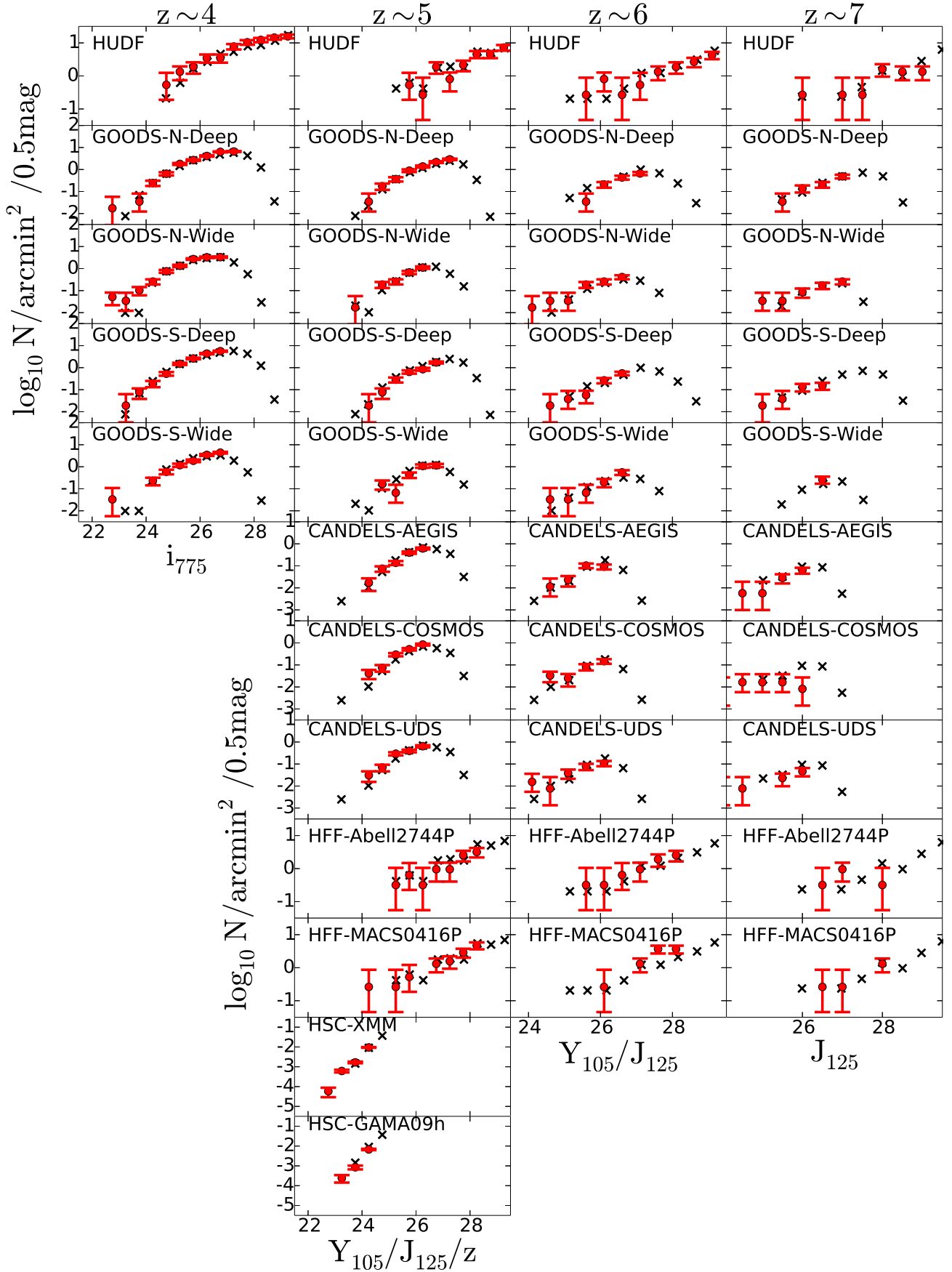


**Figure 2.** Surface number densities of LBGs at  $z \sim 4, 5, 6,$  and  $7$ . The red circles represent the surface number densities of our LBGs, while the black crosses denote the surface number densities of the LBGs presented in the literature (Bouwens et al. 2015; Hildebrandt et al. 2009). The surface number densities of our LBGs are consistent with the previous results. We confirm that the errors of our surface number densities are comparable with Bouwens et al. (2015) in HUDF.

**Table 4**  
Number of LBGs for Our Analysis

Field (1)	Area (arcmin <sup>2</sup> ) (2)	5 $\sigma$ depth (3)	$z \sim 4$ (4)	$z \sim 5$ (5)	$z \sim 6$ (6)	$z \sim 7$ (7)
HUDF	3.7	30.6	290 (348)	48 (130)	0 (86)	0 (50)
GOODS-N-Deep	57.4	28.6	1411 (1655)	431 (630)	43 (136)	81 (113)
GOODS-N-Wide	58.2	28.1	788 (800)	193 (223)	63 (69)	27 (72)
GOODS-S-Deep	52.7	29.0	1139 (1872)	205 (696)	142 (311)	66 (203)
GOODS-S-Wide	30.4	28.3	461 (510)	92 (142)	28 (51)	13 (31)
CANDELS-AEGIS	174.9	28.0	...	304 (381)	73 (101)	0 (28)
CANDELS-COSMOS	122.0	27.9	...	314 (348)	76 (80)	0 (27)
CANDELS-UDS	129.3	27.9	...	268 (310)	54 (65)	0 (25)
HFF-Abell2744P	3.1	29.3	...	30 (37)	0 (26)	0 (7)
HFF-MACS0416P	3.8	29.5	...	56 (67)	0 (53)	0 (9)
HSC-XMM	30100	25.1	...	451 (451)	...	...
HSC-GAMA09h	24800	25.0	...	279 (279)	...	...
$N_{\text{total}}(z)$			4089 (5185)	2671 (3694)	585 (978)	291 (565)
$N_{\text{total}}$				7636 (10540)		

**Note.** — Columns: (1) Field. (2) Effective area in arcmin<sup>2</sup>. (3) 5 $\sigma$  limiting magnitude in the coadd image. (3)-(7) Number of the LBGs for our analysis at each redshift that are brighter than the 5 $\sigma$  limiting magnitude in the rest-frame UV band whose central wavelength is nearest to rest-frame 1500Å. The value in parentheses is the number of LBGs in the parent sample.

To test the dependence of the clustering strength on the luminosity of the galaxies, we make subsamples that are brighter than the threshold UV magnitudes,  $m_{\text{UV,th}}$ , that are listed in Table 5. Table 5 shows the numbers of LBGs in the subsamples. Note that the numbers of the faint-magnitude subsamples are smaller than those of bright-magnitude subsamples (e.g.  $m_{\text{UV,th}} = 29.2 - 29.8$  and  $27.2 - 28.2$ ). This is because faint-magnitude subsamples are only composed of LBGs in very deep data covering a small field (e.g. HUDF). Using the UV luminosity functions of Bouwens et al. (2015), we calculate the subsamples' LBG number densities and the errors that are corrected for the incompleteness. We estimate the cosmic variance in the number densities with the bias values obtained in Section 4.2, following the procedures in Somerville et al. (2004). We include the cosmic variance uncertainties to the number density errors. The LBG number densities and the errors are presented in Table 5.

We fit the angular correlation functions with a simple power law model,

$$\omega(\theta) = A_\omega \theta^{-\beta}. \quad (28)$$

Because we obtain no meaningful constraints on  $\beta$  for most of the subsamples, we fix the value of  $\beta$  to 0.8 that is used in the previous clustering analyses (e.g., Ouchi et al. 2001, 2004b, 2010; Foucaud et al. 2003, 2010). We use Equation (28) for  $\omega_{\text{model}}(\theta)$  to determine  $IC$  (Equation 27), and obtain the best-fit  $A_\omega$  values with Equation (26).

Contaminating sources in a galaxy sample reduce  $A_\omega$  values. If contaminants have a homogeneous sky distribution, a true  $A_\omega$  is underestimated by a factor of  $(1 - f_c)^2$ , where  $f_c$  is a contamination fraction. Because contaminants are more or less clustered, a clustering amplitude multiplied by  $1/(1 - f_c)^2$  provides the upper limit value of  $A_\omega$ ,

$$A_\omega^{\text{max}} = \frac{A_\omega}{(1 - f_c)^2}. \quad (29)$$

The contamination fractions are  $f_c \sim 2, 5, 7$ , and 9% for the  $z \sim 4, 5, 6$ , and 7 LBG samples, respectively

(Bouwens et al. 2015). The corresponding  $1/(1 - f_c)^2$  values are  $\sim 1.04, 1.1, 1.2$ , and 1.2 that are significantly smaller than the statistical errors. Thus we do not apply these contamination corrections to our  $A_\omega$  estimates. Table 5 presents the best-estimate  $A_\omega$  values. In Figure 3, we plot angular correlation functions of our subsamples with the best-fit power law model.

#### 4.2. Correlation Length and Bias

An angular correlation function shows clustering properties of galaxies projected on the sky, and depends upon a combination of a galaxy redshift distribution and a galaxy spatial correlation function  $\xi_g(r)$ . The spatial correlation function is approximated by a single power law,

$$\xi_g(r) = \left(\frac{r}{r_0}\right)^{-\gamma}, \quad (30)$$

where  $r_0$  is the correlation length. We calculate correlation lengths from the amplitudes of the angular correlation functions using the Limber equation (Peebles 1980; Efstathiou et al. 1991),

$$A_\omega = C r_0^\gamma \frac{\int_0^\infty F(z) D_\theta(z)^{1-\gamma} N(z)^2 g(z) dz}{\left[\int_0^\infty N(z) dz\right]^2}, \quad (31)$$

$$g(z) = \frac{H_0}{c} (1+z)^2 \left\{1 + \Omega_m z + \Omega_\Lambda [(1+z)^{-2} - 1]\right\}^{1/2}, \quad (32)$$

$$C = \frac{\sqrt{\pi} \Gamma[(\gamma - 1)/2]}{\Gamma(\gamma/2)}, \quad (33)$$

where  $D_\theta(z)$  is the angular diameter distance and  $N(z)$  is the redshift distribution of the sample.  $F(z)$  describes the redshift dependence of  $\xi(r)$ . Assuming that the clustering pattern is fixed in comoving coordinates in the redshift range of our sample, we use the functional form  $F(z) = [(1+z)/(1+z_c)]^{-(3+\epsilon)}$  for  $\epsilon = -1.2$  (Roche & Eales 1999), where  $z_c$  is the average redshift of the sample LBGs (Section 3.1). The  $r_0$  value does not significantly depend on  $\epsilon$  over  $-3 < \epsilon < 0$ . We adopt the redshift

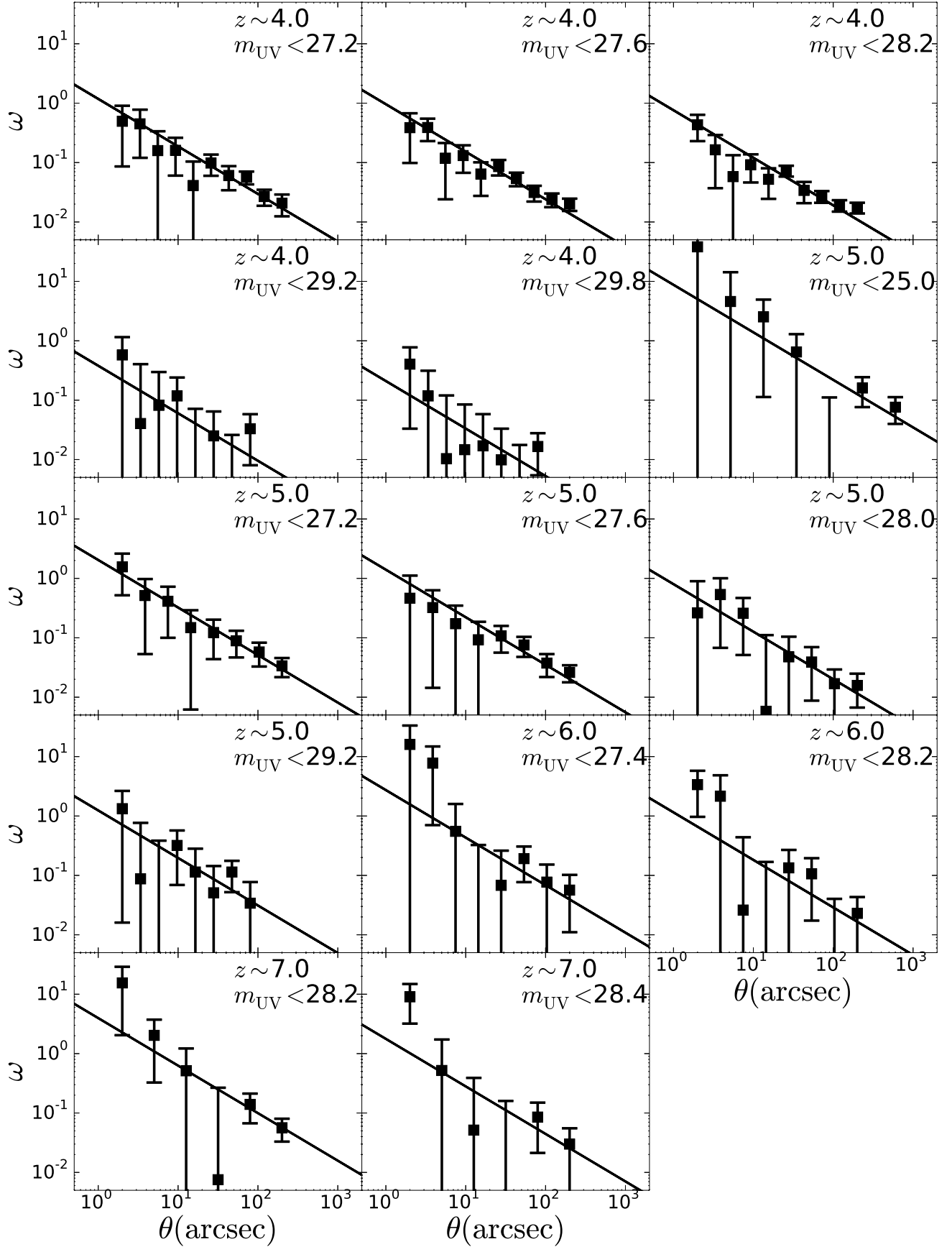


**Figure 3.** Angular correlation function of each subsample. The solid lines indicate the best-fit power law function,  $A_\omega \theta^{-\beta}$ , where we fix  $\beta = 0.8$ . The redshift and threshold magnitude are denoted at the upper right corner in each panel.

distribution of LBGs presented in Bouwens et al. (2015) and Y. Ono et al. (in preparation) for our Hubble and Subaru samples, respectively. These redshift distributions include the photometric uncertainties based on the Monte-Carlo simulations. Y. Ono et al. obtain the redshift distribution by placing artificial objects randomly in the real images using a method similar to the one in Bouwens et al. (2015). The object colors are calculated with redshifted model spectra (Bruzual & Charlot 2003) and the HSC filter response curves. We check the systematic errors on the halo mass estimates originating from the  $N(z)$  uncertainties, and find that the errors change the mass estimates negligibly, only by  $\lesssim 0.05$  dex, assuming  $\lesssim 15\%$  systematic shift of  $N(z)$  that is found in the spectroscopic results of Steidel et al. (1999).

We calculate the galaxy-dark matter bias  $b_g$  on scale of  $r = 8 h^{-1}\text{Mpc}$ , which is given by

$$b_g = \sqrt{\frac{\xi_g(r = 8 h^{-1}\text{Mpc})}{\xi_{\text{DM}}(r = 8 h^{-1}\text{Mpc}, z)}}, \quad (34)$$

where  $\xi_{\text{DM}}(r, z)$  is the spatial correlation function of the underlying dark matter calculated with the linear dark matter power spectrum,  $P_m(k, z)$ , which is defined by

$$\xi_{\text{DM}}(r, z) = \int \frac{k^2 dk}{2\pi^2} \frac{\sin(kr)}{kr} P_m(k, z). \quad (35)$$

Table 5 presents the bias values thus obtained.

#### 4.3. HOD Model

To connect observed galaxies to their host dark matter halos, we use a halo occupation distribution (HOD) model that is an analytic model of galaxy clustering (e.g., Seljak 2000; Berlind & Weinberg 2002; Cooray & Sheth 2002; Berlind et al. 2003; Kravtsov et al. 2004; Zheng et al. 2005). The HOD model is adopted not only to low-redshift galaxies (e.g., Zehavi et al. 2005; Zheng et al. 2007; van den Bosch et al. 2013; More et al. 2015), but also to high-redshift galaxies (e.g., Hamana et al. 2004; Ouchi et al. 2005; Lee et al. 2006, 2009). The key assumption of our HOD model is that the number of galaxy,  $N$ , in a given dark matter halo depends only on the halo mass,  $M_h$ . We parameterize the mean number of galaxies in dark matter halos with a mass of  $M_h$ ,  $N(M_h)$ , that is given by

$$N(M_h) = DC(N_c(M_h) + N_s(M_h)), \quad (36)$$

where  $DC$  is the duty cycle of LBG activity (see Section 1 for the definition).  $N_c(M_h)$ , and  $N_s(M_h)$  are the mean number of central and satellite galaxies, respectively. Here the LBG activity for  $DC$  is defined by the properties of galaxies that are UV-bright star-forming galaxies selected as LBGs brighter than  $m_{\text{UV,th}}$ . We assume that  $DC$  does not depend on the halo mass in each subsample, because the present data are not large enough to investigate the mass dependence of  $DC$  that hides in the statistical errors. We adopt the functional forms of  $N_c(M_h)$  and  $N_s(M_h)$  that are motivated by N-body simulations, smoothed particle hydrodynamics simulations, and semi-analytic models for low- $z$  galaxies and LBGs (e.g., Kravtsov et al. 2004; Zheng et al. 2005; Garel et al. 2015).  $N_c(M_h)$  is approximated as a step function with

a smooth transition,

$$N_c(M_h) = \frac{1}{2} \left[ 1 + \text{erf} \left( \frac{\log M_h - \log M_{\min}}{\sigma_{\log M}} \right) \right], \quad (37)$$

where  $\sigma_{\log M}$  is a transition width reflecting the scatter in the luminosity-halo mass relation.  $M_{\min}$  is the mass scale at which 50% of halos host a central galaxy. Similarly, the mean number of satellite galaxies,  $N_s(M_h)$ , follows a power law with a mass cut,

$$N_s(M_h) = N_c(M_h) \left( \frac{M_h - M_0}{M'_1} \right)^\alpha, \quad (38)$$

where  $M_0$  is the cut off mass, and  $M'_1$  ( $\alpha$ ) is the amplitude (slope) of the power law.

We calculate galaxy number densities from the HOD model with

$$n_g(z) = \int_0^\infty dM_h \frac{dn}{dM_h}(M_h, z) N(M_h), \quad (39)$$

where  $\frac{dn}{dM_h}(M_h, z)$  is the halo mass function. We use the halo mass function derived in Behroozi et al. (2013a), which is a modification of the Tinker et al. (2008) halo mass function for the high redshift universe ( $z > 2.5$ ) matching to the *Consuelo* simulation (McBride et al. 2009; see also Leauthaud et al. 2011; Behroozi et al. 2013b)<sup>18</sup>. The difference between the Behroozi et al. (2013a) and Tinker et al. (2008) halo mass functions is  $\sim 10\%$  in the number density of the  $M_h \sim 10^{10} M_\odot$  dark matter halo at  $z \sim 4 - 7$ . If we use the original mass function of Tinker et al. (2008), we find that none of our conclusions are changed.

In our HOD model,  $\xi_g(r)$  is computed from the galaxy power spectrum,  $P_g(k)$ , through the Fourier transformation,

$$\xi_g(r) = \frac{1}{2\pi^2} \int_0^\infty dk k^2 P_g(k) \frac{\sin kr}{kr}. \quad (40)$$

The galaxy power spectrum is described by

$$P_g(k) = P_g^{1h}(k) + P_g^{2h}(k), \quad (41)$$

where  $P_g^{1h}(r)$  ( $P_g^{2h}(r)$ ) is the one (two) halo term for pairs of galaxies in one (two different) halo(s).

The one-halo term consists of a central-satellite part  $P_g^{\text{cs}}(k)$  and a satellite-satellite part  $P_g^{\text{ss}}(k)$ ,

$$P_g^{1h}(k) = P_g^{\text{cs}}(k) + P_g^{\text{ss}}(k). \quad (42)$$

The quantities of  $P_g^{\text{cs}}(k)$  and  $P_g^{\text{ss}}(k)$  are given by

$$P_g^{\text{cs}}(k, z) = \frac{2}{n_g^2} \int dM_h \langle N_c N_s \rangle (M_h) \frac{dn}{dM_h}(M_h, z) u(k, M_h, z) \quad (43)$$

and

$$P_g^{\text{ss}}(k, z) = \frac{1}{n_g^2} \int dM_h \langle N_s(N_s - 1) \rangle (M_h) \frac{dn}{dM_h}(M_h, z) u^2(k, M_h, z), \quad (44)$$

<sup>18</sup> <http://lss.phy.vanderbilt.edu/lasdamas/>

**Table 5**  
Summary of the Clustering Measurements with the Power Law Model

$z_c$	$m_{\text{UV,th}}$	$M_{\text{UV,th}}$	$\langle M_{\text{UV}} \rangle$	$\log \text{SFR}_{\text{th}}$	$\log M_{*,\text{th}}$	$N$	$n_g$ ( $10^{-4} \text{ Mpc}^{-3}$ )	$A_\omega$ ( $\text{arcsec}^{0.8}$ )	$r_0$ (Mpc)	$b_g$	$\chi_\nu^2$
(1)	(2)	(3)	(4)	(5)	(6)	(7)	(8)	(9)	(10)	(11)	(12)
3.8	27.2	-19.6	-20.2	0.97	9.1	1406	$20.1 \pm 3.5$	$1.2 \pm 0.2$	$5.7^{+0.4}_{-0.4}$	$2.9^{+0.2}_{-0.2}$	0.6
	27.6	-19.2	-19.8	0.77	8.9	2301	$31.3 \pm 4.9$	$1.0 \pm 0.1$	$5.1^{+0.3}_{-0.3}$	$2.6^{+0.1}_{-0.1}$	0.8
	28.2	-18.4	-19.3	0.35	8.4	2509	$68.6 \pm 11.7$	$0.8 \pm 0.1$	$4.4^{+0.2}_{-0.2}$	$2.4^{+0.1}_{-0.1}$	1.4
	29.2	-17.3	-18.4	-0.15	7.9	161	$154.7 \pm 53.8$	$0.4 \pm 0.3$	$3.0^{+1.0}_{-1.5}$	$1.7^{+0.5}_{-0.8}$	0.4
	29.8	-16.7	-17.9	-0.49	7.5	244	$251.6 \pm 65.6$	$0.2 \pm 0.1$	$2.2^{+0.8}_{-1.0}$	$1.2^{+0.4}_{-0.5}$	0.3
4.8	25.0	-21.7	-22.1	2.0	10.2	730	$0.15 \pm 0.10$	$8.8 \pm 3.4$	$14.5^{+2.9}_{-3.5}$	$8.2^{+1.5}_{-1.8}$	0.9
4.9	27.2	-19.9	-20.5	1.0	9.1	878	$9.4 \pm 1.3$	$2.0 \pm 0.4$	$6.4^{+0.7}_{-0.7}$	$4.0^{+0.4}_{-0.4}$	0.2
	27.6	-19.5	-20.0	0.84	8.9	1467	$15.2 \pm 1.7$	$1.4 \pm 0.3$	$5.2^{+0.5}_{-0.6}$	$3.3^{+0.3}_{-0.3}$	0.4
	28.0	-19.1	-19.8	0.67	8.7	623	$22.0 \pm 3.5$	$0.8 \pm 0.3$	$3.8^{+0.7}_{-0.8}$	$2.5^{+0.4}_{-0.5}$	0.3
	29.2	-17.9	-18.7	0.011	7.9	120	$72.7 \pm 30.4$	$1.2 \pm 0.6$	$4.9^{+1.1}_{-1.4}$	$3.1^{+0.6}_{-0.8}$	0.4
	29.8	-17.3	-18.4	-0.15	7.9	161	$154.7 \pm 53.8$	$0.4 \pm 0.3$	$3.0^{+1.0}_{-1.5}$	$1.7^{+0.5}_{-0.8}$	0.4
5.9	27.4	-20.0	-20.5	1.1	9.1	285	$3.8 \pm 0.6$	$2.7 \pm 1.3$	$6.4^{+1.5}_{-1.9}$	$4.7^{+1.0}_{-1.3}$	0.6
	28.4	-19.1	-19.3	0.55	8.6	278	$13.4 \pm 2.5$	$1.1 \pm 0.7$	$3.9^{+1.2}_{-1.6}$	$3.0^{+0.8}_{-1.2}$	0.6
6.8	28.2	-19.5	-19.9	0.75	8.8	113	$7.0 \pm 2.5$	$4.0 \pm 1.2$	$8.7^{+1.4}_{-1.6}$	$7.1^{+1.0}_{-1.2}$	0.6
	28.4	-19.3	-19.8	0.65	8.7	150	$9.0 \pm 2.2$	$1.8 \pm 1.0$	$5.5^{+1.6}_{-2.2}$	$4.7^{+1.2}_{-1.7}$	0.7

**Note.** — Columns: (1) Mean redshift. (2) Threshold aperture magnitude in the rest-frame UV band. (3) Threshold absolute total magnitude in the rest-frame UV band. (4) Mean absolute total magnitude in the rest-frame UV band. (5) Threshold SFR in a unit of  $M_\odot \text{ yr}^{-1}$  derived from the threshold total magnitude,  $M_{\text{UV,th}}$ . (6) Threshold stellar mass in a unit of  $M_\odot$  derived from  $M_{\text{UV,th}}$  via equation (57), (58), (59). (7) Number of galaxies in our subsample. (8) Number density of our subsample derived from a UV luminosity function of Bouwens et al. (2015). (9) Power law amplitude (the power law index is fixed to  $\beta = 0.8$ ). (10) Spatial correlation length. (11) Galaxy-dark matter bias estimated by the power law model. See column (6) in Table 6 for the best estimate from the HOD modeling. (12) Reduced  $\chi^2$  value.

where  $u(k, M_h, z)$  is the Fourier transform of the dark matter halo density profile normalized by its mass (e.g., Cooray & Sheth 2002). Here we assume that satellite galaxies in halos trace the density profile of the dark matter halo by NFW profile (Navarro et al. 1996, 1997), and adopt the mass-concentration parameter relation by Bullock et al. (2001) with an appropriate correction (see Shimizu et al. 2003). If we assume the  $z = 4$  mass-concentration parameter relation for the halo mass estimate of the  $z \sim 7$  subsample, we find the negligible change of 0.05 dex in  $\log M_{\text{min}}$ . The values of  $\langle N_c N_s \rangle (M_h)$  and  $\langle N_s (N_s - 1) \rangle (M_h)$  are the mean number of central-satellite and satellite-satellite galaxy pairs, respectively. If we assume the independence of central and satellite galaxies and a Poisson distribution of the satellite galaxy's distribution, these values are

$$\langle N_c N_s \rangle (M_h) = N_c(M_h) N_s(M_h), \quad (45)$$

$$\langle N_s (N_s - 1) \rangle (M_h) = N_s^2(M_h). \quad (46)$$

The two-halo term is expressed as

$$P_g^{2h}(k, z) = P_m(k, z) \left[ \frac{1}{n_g} \int dM_h N(M_h) \frac{dn}{dM_h}(M, z) b_h(M_h, z) u(k, M_h, z) \right]^2, \quad (47)$$

where  $b_h(M_h, z)$  is the halo bias factor (Tinker et al. 2010).

To compare with the observational results, we calculate the angular correlation function from the galaxy power spectrum projecting on the redshift distribution using the Limber approximation (see e.g. chapter 2 of Bartel-

mann & Schneider 2001),

$$\omega(\theta) = \int dz N^2(z) \left( \frac{dr}{dz} \right)^{-1} \int dk \frac{k}{2\pi} P_g(k, z) J_0[r(z)\theta k], \quad (48)$$

where  $N(z)$  is the normalized redshift distribution of galaxies and  $J_0(x)$  is the zeroth-order Bessel function of the first kind. Here we assume that  $N_c(M)$  and  $N_s(M)$  do not vary as a function of redshift within the redshift ranges of the subsamples. The quantity  $r(z)$  is the radial comoving distance given by

$$r(z) = \frac{c}{H_0} \int_0^z \frac{dz}{\sqrt{\Omega_{m,0}(1+z)^3 + \Omega_{\Lambda,0}}}, \quad (49)$$

for a flat cosmology. The mean galaxy number density with a redshift distribution  $N(z)$  is calculated by

$$n_g = \frac{\int dz [dV(r)/dz] N(z) n_g(z)}{\int dz [dV(r)/dz] N(z)}, \quad (50)$$

where  $n_g(z)$  is defined by Equation (39), and  $dV(r)/dz$  is the comoving volume element per unit solid angle,

$$\frac{dV(z)}{dz} = r^2(z) \frac{dr}{dz}. \quad (51)$$

## 5. DARK MATTER HALO MASS

### 5.1. HOD Model Fitting

We fit our HOD model to the angular correlation function and the number density of each subsample, minimizing the  $\chi^2$  value,

$$\chi^2 = \sum_i \frac{[\omega_{\text{obs}}(\theta_i) - \omega_{\text{model}}(\theta_i)]^2}{\sigma_\omega^2(\theta_i)} + \frac{[\log n_g^{\text{obs}} - \log n_g^{\text{model}}]^2}{\sigma_{\log n_g}^2}. \quad (52)$$

We simply use the diagonal elements in the covariance matrix, in the same manner as Hamana et al. (2004) and Zheng et al. (2007), because the errors of our correlation functions are dominated by the Poisson errors due to the small number statistics. In fact, if we include off diagonal elements in the covariance matrix, changes in the best-fit value and  $1\sigma$  errors of  $\log M_{\min}$  are small,  $\sim 0.06$  dex, which does not change our conclusions.

We constrain the parameters of our HOD model using the Markov Chain Monte Carlo (MCMC) parameter estimation technique. Our HOD model has a total of 6 parameters,  $DC$ ,  $M_{\min}$ ,  $\sigma_{\log M}$ ,  $M_0$ ,  $M'_1$ , and  $\alpha$ . However, it is difficult to constrain all of these 6 parameters with our data whose statistical accuracies are not high. We thus fix  $\sigma_{\log M} = 0.2$  and  $\alpha = 1.0$ , following results of previous studies (e.g., Kravtsov et al. 2004; Zheng et al. 2005; Conroy et al. 2006). To derive  $M_0$  from  $M'_1$ , we use the relation

$$\log M_0 = 0.76 \log M'_1 + 2.3, \quad (53)$$

that is given by Conroy et al. (2006) at  $z \sim 0 - 5$  based on their simulations.

Our HOD model with 3 parameters,  $DC$ ,  $M_{\min}$ ,  $M'_1$ , is fitted to the subsamples of  $z \sim 4$  LBGs with  $m_{\text{UV},\text{th}} = 27.6 - 28.2$  whose measurements have moderately high signal-to-noise ratios. The best-fit parameters are summarized in Table 6.

Note that the rest of  $z \sim 4$  LBG subsamples with  $m_{\text{UV},\text{th}} = 27.2, 29.2$ , and  $29.8$  do not have statistical accuracies high enough to constrain  $M'_1$  that describes the small scale clustering.<sup>19</sup> We thus adopt another relation

$$\log M'_1 = 1.18 \log M_{\min} - 1.28, \quad (54)$$

that is calibrated with the results of Martinez-Manso et al. (2015). We obtain the best-fit parameters that are summarized in Table 6. In the left panels of Figure 4, we plot the angular correlation functions with the best-fit HOD model curves. The models and the data agree well. The right panels of Figure 4 are error contours in our HOD model obtained from the MCMC run.

The  $z \geq 5$  subsamples have statistical uncertainties even higher than  $z \sim 4$  subsamples. Here we calculate the mean  $DC$  value from the  $z \sim 4$  subsample fitting results to be  $DC = 0.6^{+0.2}_{-0.3}$ . Assuming that  $DC$  does not evolve by redshift, we use  $DC = 0.6$  in our model fitting for the  $z \geq 5$  subsamples. We thus obtain the  $M_{\min}$  estimates as summarized in Table 6. The errors of  $M_{\min}$  include statistical uncertainties in the fitting with  $DC = 0.6$  and uncertainties originating from the  $DC$  determination ( $DC = 0.6^{+0.2}_{-0.3}$ ). Figures 5 and 6 are the same as Figure 4, but for the  $z \geq 5$  subsamples. Because  $DC$  is fixed to  $DC = 0.6$ , the right panels of Figures 5 and 6 show the probability distributions of  $M_{\min}$ .

## 5.2. Dark matter halo Mass Estimates

From the best-fit HOD model parameters, we calculate the effective galaxy bias

$$b_g^{\text{eff}} = \frac{1}{n_g} \int dM_h \frac{dn}{dM_h}(M_h, z) N(M_h) b_h(M_h, z) \quad (55)$$

<sup>19</sup>  $M'_1$  is sensitive to the 1-halo term (see Equation (38)).

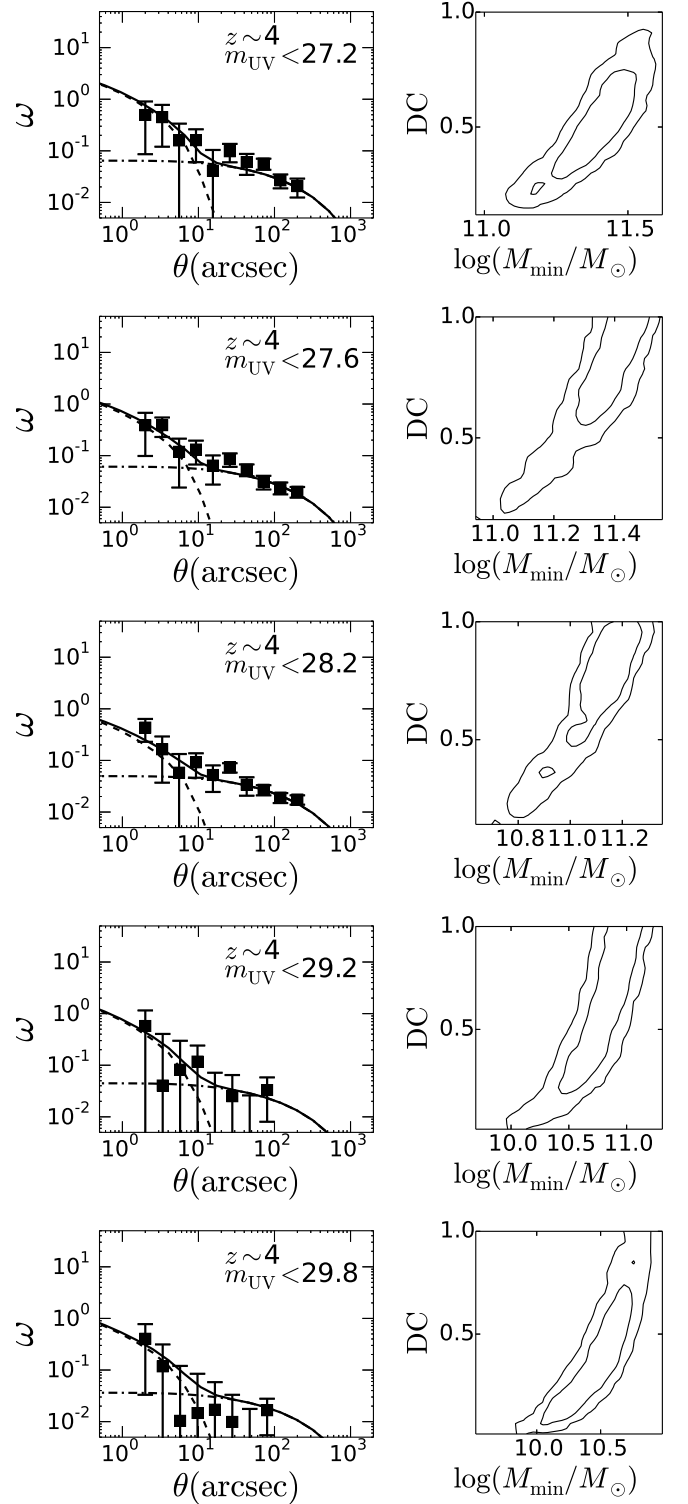


**Figure 4.** Angular correlation function and the best-fit HOD model at  $z \sim 4$ . Left panels: angular correlation function with the prediction from our best-fit HOD model. The dashed and dot-dashed curves denote the 1-halo and 2-halo terms (Equations 42 and 47), respectively. Right panels: error contour obtained from our MCMC run. The contours indicate the 68% and 95% confidence regions.

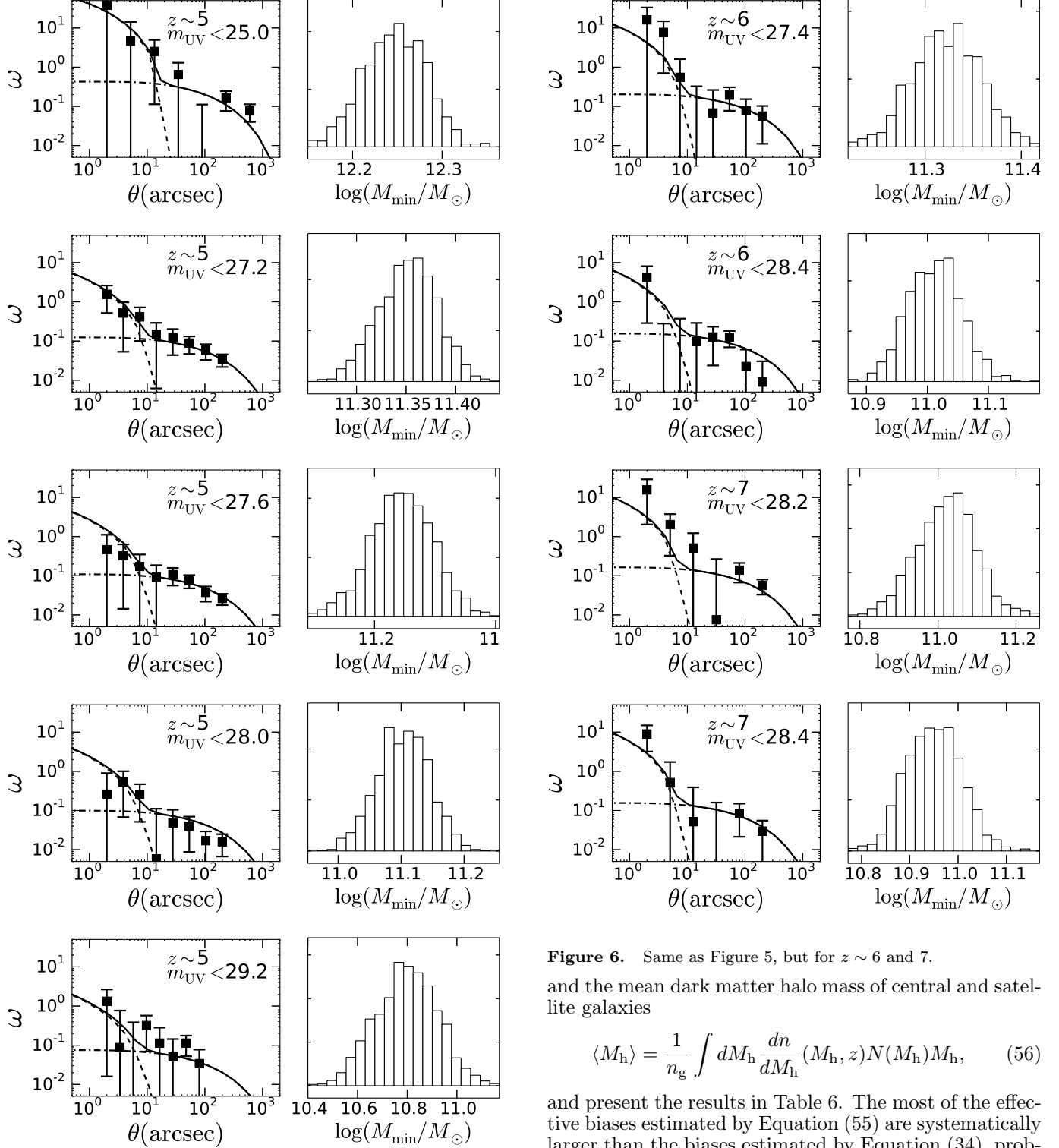


**Figure 5.** Angular correlation function and the best-fit HOD model at  $z \sim 5$ . Left panels: angular correlation function with the prediction from our best-fit HOD model. The dashed and dot-dashed curves denote the 1-halo and 2-halo terms (Equations 42 and 47), respectively. Right panels: probability distribution for  $\log M_{\min}$  obtained from our MCMC run.

**Figure 6.** Same as Figure 5, but for  $z \sim 6$  and 7.

and the mean dark matter halo mass of central and satellite galaxies

$$\langle M_h \rangle = \frac{1}{n_g} \int dM_h \frac{dn}{dM_h}(M_h, z) N(M_h) M_h, \quad (56)$$

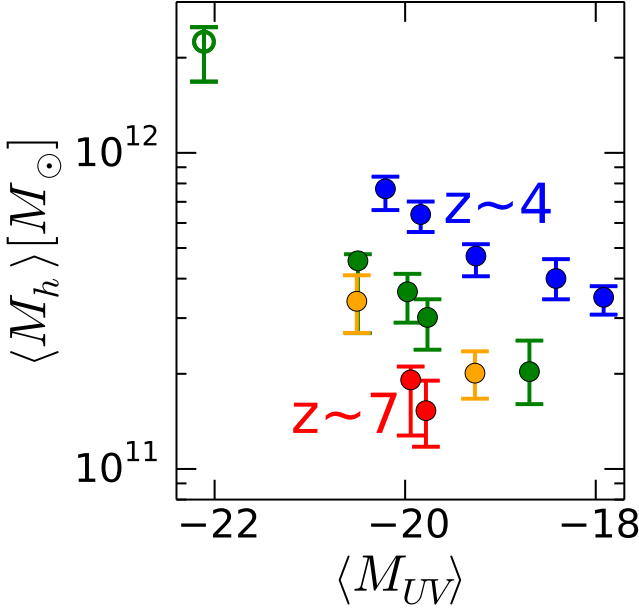
and present the results in Table 6. The most of the effective biases estimated by Equation (55) are systematically larger than the biases estimated by Equation (34), probably because the effective bias with Equation (55) is the average bias including the satellite galaxies, majority of which reside in the massive halos.

Figure 7 shows  $\langle M_h \rangle$  as a function of mean absolute UV magnitude,  $\langle M_{UV} \rangle$  that is the mean of the absolute UV magnitude of the LBG subsample. The dark matter halo masses from the Hubble data fall in the range of  $\langle M_h \rangle \sim (1 - 8) \times 10^{11} M_\odot$ , while the one from the HSC data is at the massive regime of  $\langle M_h \rangle \sim 2 \times 10^{12} M_\odot$ .

**Table 6**  
Summary of the Clustering Measurements with our HOD Model

$z_c$ (1)	$m_{UV,th}$ (2)	$\log M_{min}$ (3)	$DC$ (4)	$\log M'_1$ (5)	$b_g^{eff}$ (6)	$\log \langle M_h \rangle$ (7)	$\chi^2_\nu$ (8)
3.8	27.2	$11.42^{+0.07}_{-0.12}$	$0.50^{+0.17}_{-0.16}$	$(12.19^{+0.08}_{-0.15})$	$3.6^{+0.1}_{-0.2}$	$11.89^{+0.04}_{-0.07}$	0.9
	27.6	$11.39^{+0.05}_{-0.09}$	$0.99^{+0.01}_{-0.32}$	$12.35^{+0.20}_{-0.19}$	$3.5^{+0.1}_{-0.1}$	$11.80^{+0.04}_{-0.06}$	0.8
	28.2	$11.15^{+0.06}_{-0.13}$	$0.80^{+0.12}_{-0.29}$	$12.07^{+0.21}_{-0.28}$	$3.1^{+0.1}_{-0.1}$	$11.67^{+0.04}_{-0.06}$	1.1
	29.2	$10.78^{+0.18}_{-0.25}$	$0.95^{+0.03}_{-0.54}$	$(11.59^{+0.12}_{-0.35})$	$2.8^{+0.1}_{-0.2}$	$11.60^{+0.06}_{-0.07}$	0.8
	29.8	$10.55^{+0.14}_{-0.28}$	$0.28^{+0.33}_{-0.13}$	$(11.17^{+0.17}_{-0.33})$	$2.6^{+0.1}_{-0.1}$	$11.54^{+0.04}_{-0.05}$	1.3
	4.8	$12.25^{+0.05}_{-0.14}$	0.60 (fix)	$(13.18^{+0.06}_{-0.18})$	$7.6^{+0.3}_{-0.7}$	$12.35^{+0.05}_{-0.13}$	1.6
4.9	27.2	$11.35^{+0.05}_{-0.19}$	0.60 (fix)	$(12.12^{+0.24}_{-0.17})$	$5.0^{+0.1}_{-0.7}$	$11.66^{+0.02}_{-0.23}$	0.3
	27.6	$11.22^{+0.06}_{-0.18}$	0.60 (fix)	$(11.96^{+0.08}_{-0.20})$	$4.7^{+0.2}_{-0.4}$	$11.56^{+0.06}_{-0.10}$	0.9
	28.0	$11.11^{+0.10}_{-0.18}$	0.60 (fix)	$(11.80^{+0.11}_{-0.20})$	$4.4^{+0.2}_{-0.3}$	$11.48^{+0.06}_{-0.10}$	1.8
	29.2	$10.78^{+0.18}_{-0.24}$	0.60 (fix)	$(11.46^{+0.20}_{-0.26})$	$3.8^{+0.3}_{-0.3}$	$11.31^{+0.10}_{-0.10}$	0.5
5.9	27.4	$11.30^{+0.10}_{-0.13}$	0.60 (fix)	$(12.06^{+0.12}_{-0.16})$	$6.3^{+0.4}_{-0.4}$	$11.53^{+0.08}_{-0.10}$	0.5
	28.4	$11.03^{+0.05}_{-0.18}$	0.60 (fix)	$(11.75^{+0.07}_{-0.22})$	$5.5^{+0.2}_{-0.4}$	$11.30^{+0.07}_{-0.08}$	1.4
6.8	28.2	$11.04^{+0.08}_{-0.22}$	0.60 (fix)	$(11.77^{+0.07}_{-0.28})$	$6.8^{+0.2}_{-0.8}$	$11.28^{+0.04}_{-0.18}$	0.9
	28.4	$10.99^{+0.06}_{-0.20}$	0.60 (fix)	$(11.69^{+0.07}_{-0.27})$	$6.3^{+0.4}_{-0.4}$	$11.18^{+0.09}_{-0.11}$	0.6

**Note.** — Columns: (1) Mean redshift. (2) Threshold magnitude in the rest-frame UV band. (3) Best-fit value of  $M_{min}$  in a unit of  $M_\odot$ . (4) Star formation duty cycle. (5) Best-fit value of  $M'_1$  in a unit of  $M_\odot$ . The value in parentheses is derived from  $\log M_{min}$  via equation (54). (6) Effective bias. (7) Mean halo mass in a unit of  $M_\odot$ . (8) Reduced  $\chi^2$  value.



**Figure 7.** Mean dark matter halo mass as a function of mean absolute UV magnitude. The blue, green, orange, and red circles represent the mean dark matter halo mass of our Hubble subsample at  $z \sim 4, 5, 6$ , and  $7$ , respectively. The open green circle denotes the mean dark matter halo mass of our subsample constructed from the HSC data.

There is a trend of increasing the dark matter halo mass with increasing the UV luminosity at all redshifts. Our results suggest that more UV luminous LBGs reside in more massive dark matter halos, and agree with the conclusions of previous high- $z$  galaxy studies (Ouchi et al. 2001, 2004b, 2005; Foucaud et al. 2003; Lee et al. 2006; Barone-Nugent et al. 2014).

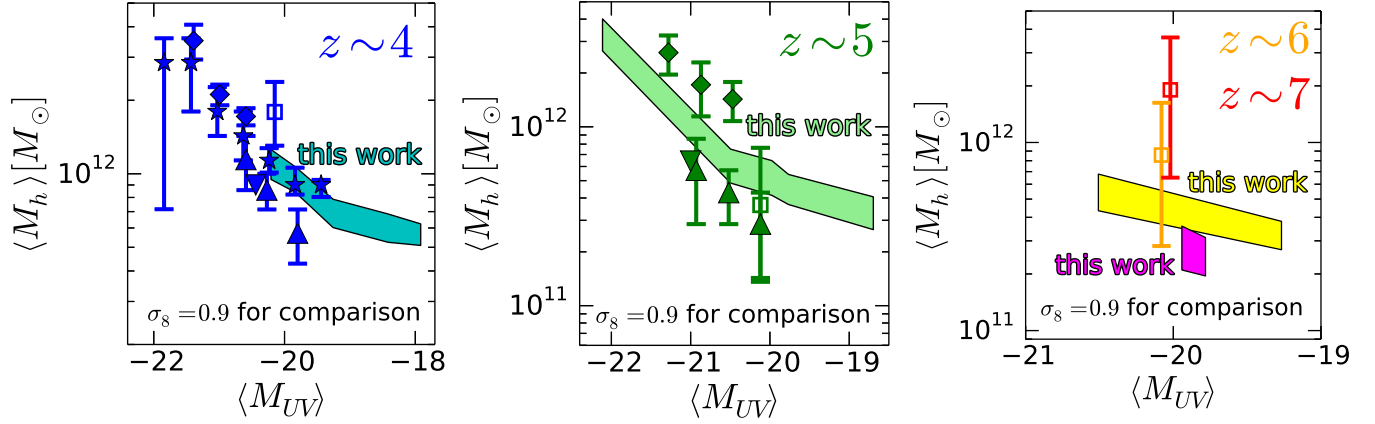
### 5.3. Comparison with Previous Clustering Studies

Figure 8 compares our results with previous clustering studies (Hamana et al. 2004; Ouchi et al. 2005; Lee et al. 2006; Hildebrandt et al. 2009; Barone-Nugent et al. 2014). Because most of the previous studies assume  $\sigma_8 = 0.9$  that is different from our assumption ( $\sigma_8 = 0.8$ ), we obtain our HOD model fitting results for our data with  $\sigma_8 = 0.9$  for comparison. Similarly, the previous study results are re-calculated with the cosmological parameter sets with  $\Omega_m = 0.3$ ,  $\Omega_\Lambda = 0.7$ ,  $H_0 = 70 \text{ km s}^{-1} \text{ Mpc}^{-1}$ , and  $\sigma_8 = 0.9$ . In this way, we conduct our comparisons with the same cosmological parameter set for our and the previous studies' results. In Figure 8, we find that our  $z \sim 4$  results are consistent with those of the previous studies within the uncertainties (see also Park et al. 2015). Although the previous  $z \sim 5$  results are largely scattered, our  $z \sim 5$  results are placed near the center of the distribution of the previous study data points. At  $z \sim 6$ , again our result agrees with the one of Barone-Nugent et al. (2014). We confirm that our  $z \sim 4 - 6$  results are consistent with those of the previous studies. At  $z \sim 7$ , there is a  $1 - 2\sigma$  difference between our results and those in Barone-Nugent et al. (2014). This difference may be simply explained by the measurement uncertainties or the difference of the LBG sample selections. As shown in Figure 8, we estimate the dark matter halo mass at  $z \sim 6 - 7$  for the first time by the clustering analysis with the HOD model (c.f., Barone-Nugent et al. 2014, by no HOD modeling).

## 6. SHMR

### 6.1. Stellar Mass Estimates

We estimate stellar masses  $M_*$  of our LBGs with the Chabrier (2003) IMF from UV magnitudes  $M_{UV}$ , exploiting the star-formation main sequence, a tight correlation between  $M_*$  and star-formation rate (SFR) found at high- $z$  (e.g., Daddi et al. 2007). Because LBGs at



**Figure 8.** Comparison with previous clustering studies under the same cosmology,  $\sigma_8 = 0.9$ . Our results are recalculated with  $\sigma_8 = 0.9$ . Left panel: comparison at  $z \sim 4$ . The cyan shaded region represents the mean dark matter halo mass of our subsample at  $z \sim 4$ . The blue symbols represent the results of the previous studies. We plot the results of Hamana et al. (2004, downward triangle), Ouchi et al. (2005, stars), Lee et al. (2006, upward triangles), and Hildebrandt et al. (2009, diamonds). The downward triangle has no error bar, because Hamana et al. (2004) do not provide errors of the mean dark matter halo mass. We also show the results of Barone-Nugent et al. (2014) as a blue open square, who use the simple power law model. Center panel: comparison at  $z \sim 5$ . The light green shaded region represents the mean dark matter halo mass of our subsample at  $z \sim 5$ . The green symbols represent the results of the previous studies of Hamana et al. (2004, downward triangle), Lee et al. (2006, upward triangles), Hildebrandt et al. (2009, diamonds), and Barone-Nugent et al. (2014, open square). Right panel: comparison at  $z \sim 6, 7$ . The yellow and magenta shaded regions represent the mean dark matter halo masses of our subsample at  $z \sim 6$ , and 7, respectively. The orange and red open squares represent the results of Barone-Nugent et al. (2014) at  $z \sim 6$ , and 7, respectively.

$z \gtrsim 4$  are generally very dust poor, SFR well correlates with  $M_{UV}$ . Thus,  $z \gtrsim 4$  LBGs have a correlation between  $M_{UV}$  and  $M_*$ . We use the  $M_{UV} - M_*$  relations in Shibuya et al. (2015). These are the empirical  $M_{UV} - M_*$  relations at  $z = 0 - 6$  with photo- $z$  galaxies in the 3D-HST catalog in Skelton et al. (2014), who carry out the SED fitting for the stellar mass with the Salpeter (1955) IMF. In order to convert our stellar mass estimates of Salpeter (1955) to Chabrier (2003) IMFs, our final estimates are divided by a factor of 1.8. We thus estimate  $M_*$  from  $M_{UV}$  with the relations,

$$\log M_* = -1.16 - 0.54 \times M_{UV} \quad (z \sim 4) \quad (57)$$

$$\log M_* = -2.28 - 0.59 \times M_{UV} \quad (z \sim 5) \quad (58)$$

$$\log M_* = -2.45 - 0.59 \times M_{UV} \quad (z \sim 6, 7). \quad (59)$$

Because Shibuya et al. (2015) show the  $M_{UV} - M_*$  relations in the redshift ranges of  $z = 3 - 4$ ,  $4 - 5$ , and  $5 - 6$ , we interpolate the relations in Shibuya et al. (2015) by redshift to derive Equations (57) and (58) for  $z \sim 4$  and 5 LBGs, respectively. For  $z \sim 6$  and 7 LBGs, we use the  $M_{UV} - M_*$  relation of  $z \sim 5 - 6$  given in Shibuya et al. (2015). If we extrapolate the  $M_{UV} - M_*$  relation to  $z \sim 6$  and 7, the derived stellar mass at  $M_{UV} = -20$  becomes larger by 0.1 dex at  $z \sim 6$  and by 0.3 dex at  $z \sim 7$ , which do not change our conclusions (Section 6.2). We also confirm that our conclusions do not change, if we use the  $M_{UV} - M_*$  relations of Song et al. (2015). Note that the uncertainty of the best-fit relations (the scatter of the stellar masses) is typically  $< 0.01$  dex (0.5 dex). In Table 5, we present estimates of the stellar masses  $M_{*,th}$  that correspond to the threshold UV magnitudes,  $M_{UV,th}$ , of the subsamples.

### 6.2. SHMRs and the Evolution

Figure 9 presents SHMRs of central galaxies for our LBG subsamples at  $z \sim 4, 5, 6$ , and 7. Hereafter, we

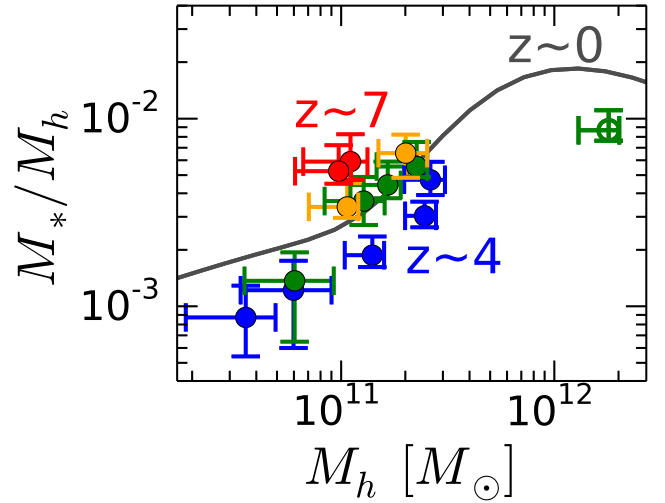


**Figure 9.** SHMR of central galaxies as a function of dark matter halo mass at  $z \sim 4, 5, 6$ , and 7. The blue, green, orange, and red circles represent the SHMR of our Hubble subsample at  $z \sim 4, 5, 6$ , and 7, respectively. The open green circle denotes the SHMR of our subsample constructed from the HSC data. The gray solid curve is the SHMR of Behroozi et al. (2013a) at  $z \sim 0$ , which is computed by P. Behroozi with the same cosmological parameters and stellar mass estimate as our analysis.

use  $M_{*,th}$  and  $M_{min}$  values for stellar masses  $M_*$  and halo masses  $M_h$ , respectively, because these quantities define our subsamples in a self-consistent manner. The black curve in Figure 9 represents the SHMR function at  $z \sim 0$  that is the same as the one of Behroozi et al. (2013a), but for our cosmological parameters and stellar-mass estimate assumptions (P. Behroozi, private communication).

In Figure 9, the combination of the Hubble and HSC data covers the wide halo mass range of  $6 \times 10^{10} - 2 \times$

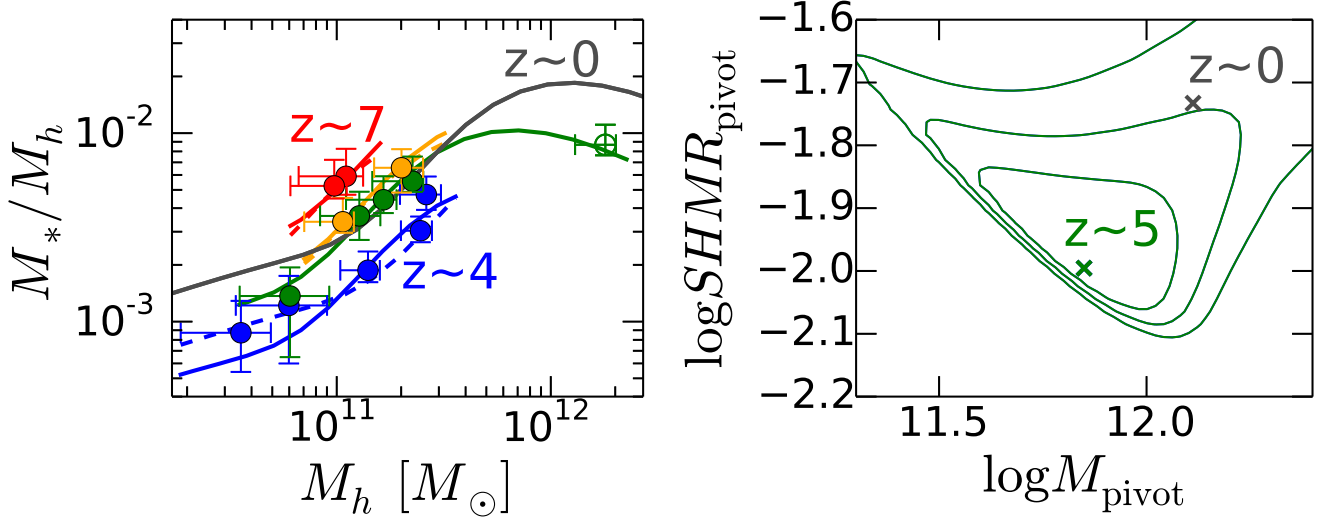


**Figure 10.** SHMR evolution. The left panel shows the results of our SHMR function fittings. The green curve represents the best-fit SHMR function at  $z \sim 5$ . We fit SHMR functions to our  $z \sim 5$  SHMR- $M_h$  data (green circles) by parametrizing the  $z \sim 0$  SHMR function of Behroozi et al. (2013a) with a pivot mass,  $M_{\text{pivot}}$ , and an SHMR amplitude at the pivot mass,  $SHMR_{\text{pivot}}$ . The blue, orange, and red solid (dashed) curves describe the best-fit SHMR functions of  $z \sim 4, 6$ , and  $7$ , respectively, in the  $M_{\text{pivot}}$ -fixed ( $SHMR_{\text{pivot}}$ -fixed) case. These curves are shown only in the range where measurements are available. The details of the fitting are presented in Section 6.2. In the right panel, the green contours represent the 1.0, 1.5 and  $2.0\sigma$  confidence levels of  $M_{\text{pivot}}$  and  $SHMR_{\text{pivot}}$  at  $z \sim 5$ . The green cross in the contours corresponds to the best-fit values at  $z \sim 5$ . The gray cross shows the values of  $M_{\text{pivot}}$  and  $SHMR_{\text{pivot}}$  at  $z \sim 0$  (Behroozi et al. 2013a).

$10^{12} M_\odot$  at  $z \sim 5$ . The SHMR increases from  $\sim 10^{-3}$  to  $\sim 10^{-2}$ , with increasing  $M_h$  from  $\sim 6 \times 10^{10}$  to  $\sim 2 \times 10^{12} M_\odot$  at  $z \sim 5$ . Similar positive correlations are found in the SHMR- $M_h$  relations at  $z \sim 4$  and  $6$  as well as  $z \sim 0$ . The SHMRs at  $z \sim 7$  are consistent with the positive correlation. At low redshift ( $z \lesssim 1$ ), this correlation is claimed in various studies (e.g., Leauthaud et al. 2012; Coupon et al. 2015). Our results newly show the positive correlations of SHMR- $M_h$  near  $M_h \sim 10^{11} M_\odot$  at high redshift,  $z \sim 4 - 6$ .

At  $z = 0 - 7$ , the SHMR values at  $M_h \sim 10^{11}$  are obtained, which allow us to investigate evolution of SHMRs. From  $z \sim 0$  to  $z \sim 4$ , the SHMR decreases by a factor of  $\sim 3$ , from  $\sim 3 \times 10^{-3}$  to  $\sim 1 \times 10^{-3}$ . In contrast to the evolution from  $z \sim 0$  to  $z \sim 4$ , the SHMR increases by a factor of  $\sim 5$ , from  $\sim 1 \times 10^{-3}$  at  $z \sim 4$  to  $\sim 5 \times 10^{-3}$  at  $z \sim 7$ . To quantify the evolution of the SHMR- $M_h$  relation, we parameterize the  $z \sim 0$  SHMR function of Behroozi et al. (2013a) with a pivot halo mass  $M_{\text{pivot}}$  and an SHMR amplitude at the pivot halo mass,  $SHMR_{\text{pivot}}$ ,

$$\begin{aligned} & \log(SHMR - SHMR_{\text{pivot}}) \\ &= \log \left[ \frac{M_*(M_h - M_{\text{pivot}})}{M_h - M_{\text{pivot}}} \right] \\ &= \log \left( \frac{\epsilon M_1}{M_h - M_{\text{pivot}}} \right) + f \left[ \log \left( \frac{M_h - M_{\text{pivot}}}{M_1} \right) \right] - f(0), \end{aligned} \quad (60)$$

$$f(x) = -\log(10^{\alpha x} + 1) + \delta \frac{\{\log[1 + \exp(x)]\}^\gamma}{1 + \exp(10^{-x})}, \quad (61)$$

where  $\log \epsilon = -1.85$ ,  $\log M_1 = 11.50$ ,  $\alpha = -1.39$ ,  $\delta = 3.76$ , and  $\gamma = 0.33$  at  $z \sim 0$  (P. Behroozi in private communication). We fit this parameterized SHMR function to our SHMR- $M_h$  data of the  $z \sim 4 - 7$  LBGs.

Removing the dependent results of our  $m_{\text{UV,th}}$  subsamples whose bright LBGs are repeatedly included in the subsamples, except for the HSC and some HUDF data, we only use the independent SHMR data in our fitting.

We use the subsamples of  $m_{\text{UV}} < 27.6$  mag and  $m_{\text{UV}} < 29.8$  mag ( $m_{\text{UV}} < 25.0$  mag,  $m_{\text{UV}} < 28.0$  mag, and  $m_{\text{UV}} < 29.2$  mag) for  $z \sim 4$  ( $z \sim 5$ ). Similarly, the  $m_{\text{UV}} < 28.4$  subsamples are fitted for  $z \sim 6, 7$ .

Because our  $z \sim 5$  SHMR estimates are obtained in the wide halo mass range that allows us to investigate the SHMR and  $M_h$  evolution simultaneously, we perform fitting to the  $z \sim 5$  SHMR estimates with the SHMR function varying  $M_{\text{pivot}}$  and  $SHMR_{\text{pivot}}$ . The best-fit function and the error contours are presented in the left and right panels of Figure 10, respectively. We compare these results with those at  $z \sim 0$  obtained by Behroozi et al. (2013). The left panel of Figure 10 indicates that the SHMRs of  $z \sim 0$  and  $5$  are similar at  $M_h \sim 10^{11} M_\odot$ , but different at  $M_h \sim 10^{12} M_\odot$ . The massive end of our data makes a difference in the fitting result shown in the right panel of Figure 10.

Although the mass ranges of our SHMR data are limited, the SHMR results of  $z \sim 4$  and  $7$  show large differences from those of  $z \sim 0$  at  $M_h \sim 10^{11} M_\odot$ . We quantify the differences by two extreme scenarios of  $M_{\text{pivot}}$ -fixed and  $SHMR_{\text{pivot}}$ -fixed cases that bracket the realistic scenario including both  $M_{\text{pivot}}$  and  $SHMR_{\text{pivot}}$  evolutions. Adopting the best-fit  $M_{\text{pivot}}$  or  $SHMR_{\text{pivot}}$  value at  $z \sim 5$ , we carry out the SHMR function fitting in these two cases. The left panel of Figure 10 presents the best-fit SHMR functions for  $M_{\text{pivot}}$ -fixed and  $SHMR_{\text{pivot}}$ -fixed cases with the solid and dashed lines, respectively. These two cases show very similar best-fit SHMR functions in the left panel of Figure 10, because the  $M_h$  ranges for the fitting are narrow and limited to  $M_h \sim 10^{11} M_\odot$ . Moreover, the notable differences

between  $z \sim 0$ , 4, and 7 curves are identified, suggesting the evolution of SHMR and/or  $M_h$  from  $z \sim 0$  to  $z \sim 4$  ( $z \sim 0 - 4$ ) and  $z \sim 4$  to  $z \sim 7$  ( $z \sim 4 - 7$ ). In the  $M_{\text{pivot}}$ -fixed ( $SHMR_{\text{pivot}}$ -fixed) case, the differences of  $z \sim 0 - 4$  and  $z \sim 4 - 7$  are found at the  $4.9$  and  $3.1\sigma$  ( $2.9$  and  $2.5\sigma$ ) levels, respectively. We also investigate  $M_{*,\text{pivot}}$ -fixed case with varying  $M_{\text{pivot}}$ , where  $M_{*,\text{pivot}}$  is the pivot *stellar* mass that is not the pivot *halo* mass of  $M_{\text{pivot}}$ . We find the differences at the redshift ranges of  $z \sim 0 - 4$  and  $z \sim 4 - 7$  are  $4.2$  and  $2.7\sigma$  significance levels, respectively. In addition, we adopt the best-fit  $M_{\text{pivot}}$  or  $SHMR_{\text{pivot}}$  value of  $z \sim 0$ , instead of  $z \sim 5$ , and confirm that the arguments above are unchanged. In any cases of these scenarios, we find the SHMR evolutions at the redshift ranges of  $z \sim 0 - 4$  and  $z \sim 4 - 7$  at the  $> 99\%$  and  $> 98\%$  confidence levels, respectively. These SHMR evolutionary trends at  $z \sim 0 - 4$  and  $z \sim 4 - 7$  are identified, for the first time, based on the clustering analyses.

We examine whether these results are produced by systematic biases in our HOD model fitting, where we fixed some parameters and the analytic relations. Firstly, we have assumed the fixed parameter of  $\sigma_{\log M} = 0.2$  over  $z = 4 - 7$  in Section 5, although it is known that  $\sigma_{\log M}$  could vary with the redshift and the halo mass. According to the formulation of Behroozi et al. (2013a),  $\sigma_{\log M}$  values of  $z \sim 4$  and 7 galaxies of  $M_h \sim 10^{11} M_\odot$  are 0.3 and 0.5, respectively. Adopting  $\sigma_{\log M} = 0.3$  for our  $z \sim 4$  LBGs, we find negligible differences from the original  $\sigma_{\log M} = 0.2$  results in the SHMR evolution from  $z \sim 0$  to 4. We also estimate SHMR and  $M_h$  values with  $\sigma_{\log M} = 0.5$  for our  $z \sim 7$  LBGs. Although the estimated  $M_h$  values are larger than those of the original  $\sigma_{\log M} = 0.2$  results by a factor of 1.5, the SHMR evolution from  $z \sim 4$  to 7 is still found at the  $\sim 2\sigma$  significance level. Secondly, we have adopted the analytic relations of Equations (53) and (54) to derive  $M_0$  and  $M'_1$  in Section 5. Here we fit our angular correlation functions with varying  $M_0$  and  $M'_1$  as free parameters in the ranges of  $9 < \log M'_1 < 14$  and  $8 < \log M_0 < 14$ , respectively, to evaluate the impacts of the  $M_0$  and  $M'_1$  values on our results. For all subsamples that we use in the SHMR evolution discussion, we find that the new  $M_{\text{min}}$  values from these fitting analyses agree with our best-estimate values (Table 6) within the uncertainties. For example, the subsample of  $z \sim 4$   $m_{\text{UV}} < 27.6$  mag gives the new  $M_{\text{min}}$  value of  $\log M_{\text{min}} = 11.4^{+0.1}_{-0.1}$  that is consistent with our best-estimate value of  $\log M_{\text{min}} = 11.4^{+0.1}_{-0.1}$  (Table 6). Although some errors of the new  $M_{\text{min}}$  value are larger than those of the best-estimate value by a factor of  $\sim 1.5$ , the SHMR evolution at  $z \sim 0 - 4$  is still found at the  $> 3\sigma$  level due to the scatter of the new  $M_{\text{min}}$  value that separates the SHMRs of  $z \sim 0$  and  $z \sim 4$ . The evolutions of the SHMR we find are more significant than the systematic biases.

## 7. DISCUSSION

### 7.1. Interpretations of the SHMR evolution

Figure 10 shows the redshift evolution of the SHMR at  $z \sim 0 - 7$  (Section 6.2). At the dark matter halo mass of  $\sim 10^{11} M_\odot$ , SHMRs decrease from  $z \sim 7$  to 4 by 0.7 dex, and increase from  $z \sim 4$  to 0 by 0.5 dex. These two evolutionary trends of  $\sim 10^{11} M_\odot$  dark matter halos

suggest that the stellar mass assembly is very (moderately) efficient at  $z \gtrsim 7$  ( $z \sim 0 - 4$ ), while it is inefficient at  $z \sim 4 - 7$ . There are three possible physical origins to explain the increase and decrease of SHMRs.

The first is the evolution of the gas cooling efficiency. The gas cooling efficiency is expected to be high if the number density or the chemical abundance of gas are high. At high redshift, the average density of the collapsed dark matter halos is very high due to the high cosmic matter density. Towards low redshift, the interstellar medium in galaxies becomes chemically enriched. If one tries to explain the SHMR evolution at  $M_h \sim 10^{11} M_\odot$  by the change of the gas cooling efficiency, the high SHMR at  $z \sim 7$  would be reduced by the decreasing gas cooling efficiency due to the small number density at  $z \sim 4$ . In fact, Figure 7 indicates that low-redshift galaxies tend to have a high  $\langle M_{\text{UV}} \rangle$  (i.e. low SFR) for a given  $\langle M_h \rangle$ . From  $z \sim 4$  to  $z \sim 0$ , the SHMR may increase due to the increase of gas cooling efficiency originated from the chemical enrichment.

The second is the evolution of feedback strengths. Because the mass of  $\sim 10^{11} M_\odot$  falls in a moderately low mass regime, the SN and radiation pressure feedback are probably more important than AGN feedback (e.g., Okamoto et al. 2014). Typical LBGs at  $z \gtrsim 7$  are very compact, having a half-light radius of  $\lesssim 1$  kpc (e.g. Shibuya et al. 2015). The gravitational potential at the dark matter halo center dominated by baryonic mass (Erb et al. 2006) is deeper at  $z > 7$  than  $z \sim 4 - 7$ . At  $z \sim 4 - 7$ , due to the moderately shallow gravitational potential, hot/warm gas is expelled from the center to the outer halo, and it takes time for the gas to come back to the central region by radiative cooling in the low-density regime of the outer halo. Although these dense and compact galaxies would allow the high SHMR values, the energy production rates corresponding to SFRs are also high (see Figure 8 and the discussion above). Thus, it is unclear whether feedback is responsible for the SHMR evolution at  $z > 4$ . Below  $z \sim 4$ , the decrease of specific SFRs (sSFR; SFR divided by stellar mass) is accelerated towards low- $z$  (Whitaker et al. 2014). This fast decrease of sSFR as well as the increase of the galaxy half-light radius towards low- $z$  do not raise SHMRs at  $z = 0 - 4$ . Thus, the feedback may not be major physical origins of the SHMR evolution of  $z \sim 0 - 4$ .

The third is the evolution of merger rates and merger-induced star-formation activities. In Section 6.2, we find that the SHMR positively correlates with  $M_h$  at  $\sim 10^{11} M_\odot$  over  $z \sim 0 - 7$  (Figure 9). The shape of the SHMR- $M_h$  function at  $z \sim 0$  suggests that these positive correlations at  $z \sim 0 - 7$  continue to a halo mass range much lower than  $M_h$  at  $\sim 10^{11} M_\odot$ . If a merger is not associated with the star-formation activity (i.e. dry merger), such a merger does not change the SHMR, but increase the halo mass. For example, if a galaxy with  $\sim 10^{11} M_\odot$  forms by multiple mergers of  $\sim 10^{10} M_\odot$  galaxies with no merger induced star-formation activity, the SHMR of the  $\sim 10^{11} M_\odot$  galaxy is as low as those of the  $\sim 10^{10} M_\odot$  galaxies. Under the condition of the positive correlation between SHMR and  $M_h$ , this mechanism of mergers suppresses SHMRs. On the other hand, intensive star-formation is followed by merger events. Such a merger-induced star-formation would build up stellar masses, and boost SHMRs. Thus, there are two effects of

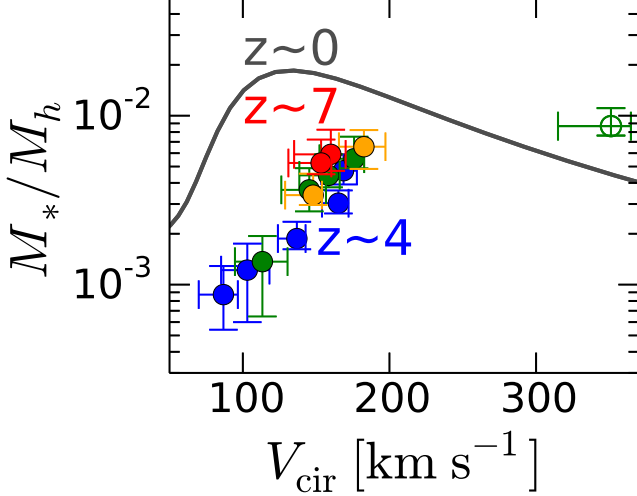


**Figure 11.** SHMR as a function of circular velocity. The blue, green, orange, and red circles represent the SHMRs of our subsamples at  $z \sim 4, 5, 6$ , and  $7$ , respectively. The gray solid curve is the SHMR of Behroozi et al. (2013a) at  $z \sim 0$ .

mergers: increasing and decreasing SHMRs. It is known that the merger rates decrease from high- $z$  to low- $z$  in simulations (Fakhouri et al. 2010). If one tries to explain the SHMR evolution at  $\sim 10^{11} M_\odot$  by merger alone, the high SHMR raised by merger-induced star formation may be reduced by the decrease of the merger rate. At  $z \sim 0 - 4$ , the merger induced star-formation should increase SHMRs faster than the merger suppression. Here we have discussed the three possible physical origins of the SHMR evolution at  $z \sim 0 - 7$ . Although our observational results alone cannot determine what is the major physical origins, it is likely that the mixture of these effects give the evolutionary trends of the SHMRs.

We discuss this SHMR evolution with the circular velocity,

$$V_{\text{cir}} = \sqrt{\frac{GM_h}{r_{200}}}. \quad (62)$$

Since the circular velocity is determined by the halo mass and radius,  $V_{\text{cir}}$  provides the condition for gas escaping from the halo by outflow. Figure 11 presents the SHMRs as a function of circular velocity for the  $z \sim 4 - 7$  LBGs. In Figure 11, the SHMRs of  $z \sim 7$  are higher than those of  $z \sim 4$  by 0.3 dex at  $V_{\text{cir}} \sim 160 \text{ km s}^{-1}$ . This increase is smaller than the 0.7 dex increase of the SHMR from  $z \sim 4$  to  $7$  at  $M_h \sim 10^{11} M_\odot$  (Figure 10). Because the circular velocity for a given halo mass increases by redshift, the 0.7 dex SHMR evolution in the SHMR- $M_h$  plane (Figure 10) is narrowed in the SHMR- $V_{\text{cir}}$  plane (Figure 11). The small SHMR evolution in the SHMR- $V_{\text{cir}}$  plane would indicate that the ( $V_{\text{cir}}$ -dependent) gas outflow conditions are similar over the redshift range of  $z \sim 4 - 7$ . In the SHMR- $V_{\text{cir}}$  plane (Figure 11), there is a significant SHMR evolution of 0.5-1 dex at  $z \sim 0 - 4$  in contrast with the small SHMR evolution at  $z \sim 4 - 7$ . This significant SHMR evolution at  $z \sim 0 - 4$  suggests that the early galaxies at  $z \sim 4 - 7$  have the gas outflow conditions clearly different from those of matured galaxies at  $z \sim 0$ .

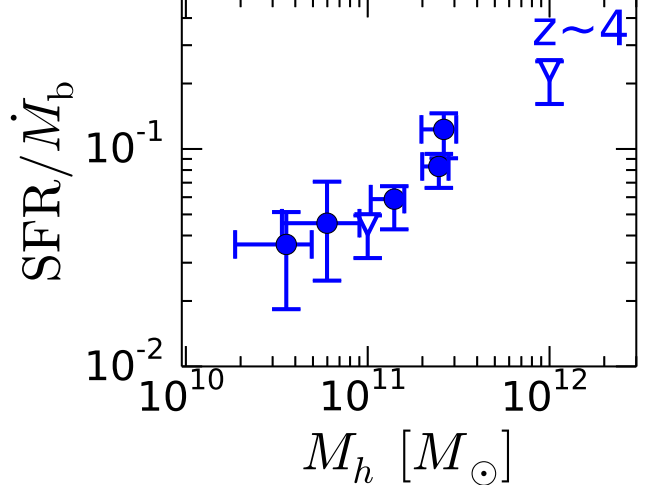


**Figure 12.** BCE as a function of dark matter halo mass at  $z \sim 4$ . The blue circles represent the BCEs of our subsample at  $z \sim 4$ . The open blue triangles at  $M_h = 10^{11}$  and  $10^{12} M_\odot$  describe the BCEs of Behroozi et al. (2013a) at  $z \sim 4$ .

## 7.2. Baryon Conversion Efficiency

In Section 6.2, we find that SHMR and  $M_h$  at  $z \sim 0 - 7$  have the positive correlations in the mass range around  $M_h \sim 10^{11} M_\odot$  (Figure 9). To understand more details of these positive correlations, we calculate the baryon conversion efficiency (BCE) of the  $z \sim 4$  subsamples that have high statistical accuracies. BCE is the ratio of the SFR to the baryon accretion rate,  $\dot{M}_b$ :

$$BCE = \frac{SFR}{\dot{M}_b}. \quad (63)$$

Because most of the accreting baryon have a form of gas (e.g., Scoville et al. 2015), we adopt  $\dot{M}_g \simeq \dot{M}_b$ . Thus, Equation (63) can be written as follows,  $BCE \simeq SFR/\dot{M}_g$ , indicating that BCE is the conversion rate from gas to stars.

We define the cosmic baryon fraction,  $f_b \equiv \Omega_b/\Omega_m = 0.15$ . The baryon accretion rate is computed with  $f_b$  by

$$\dot{M}_b = f_b \times \dot{M}_h, \quad (64)$$

where  $\dot{M}_h$  is the median halo mass accretion rate that is a function of halo mass and redshift. We estimate  $\dot{M}_h$  with the analytic formula obtained from the N-body simulation results (Behroozi et al. 2013a).

Figure 12 presents BCEs of our  $z \sim 4$  subsamples as a function of the dark matter halo mass. The errors of these BCE estimates do not include the halo mass accretion rate scatters, but the halo mass estimates. Although there exist moderately large uncertainties in the results of our  $z \sim 4$  subsamples in Figure 12, there is a signature of positive correlation between BCE and  $M_h$ . We compare BCE estimates of Behroozi et al. (2013a) in Figure 12, and confirm that our results including the positive correlation signature are consistent with those of Behroozi et al. (2013a). This consistency would indicate that the abundance matching technique provides results similar to our clustering analysis (see Section 7.3).

This positive correlation signature indicates the low

conversion efficiency from gas to stars in low-mass halos, suggesting the inefficient star formation in the low-mass halos. The inefficient star-formation probably originates from the mass dependence of feedback and/or gas cooling. In low-mass halos, star-formation activities associated with supernovae, stellar wind, and radiation produce outflowing gas that suppress next generation star formation as the feedback process. Moreover, in low-mass halos, the gas cooling is slow (Silk & Wyse 1993). The combination of these effects would make the positive correlation between BCE and  $M_h$ .

### 7.3. Comparisons with Abundance Matching Studies

#### 7.3.1. Impact of DC and HOD Systematics on the $M_h$ Estimates

We discuss differences between our clustering analysis and the abundance matching results. As explained in Section 1, these differences should originate from DC and the subhalo-galaxy relation that are implemented in our HOD model. We investigate the physical impacts of DC and HOD (which affects the subhalo-galaxy relation) on the  $M_h$  estimates, comparing those obtained from a simple abundance matching (SiAM) method based on halo mass functions of Behroozi et al. (2013a) and UV luminosity functions of Bouwens et al. (2015) at  $z \sim 4$ . We calculate  $M_h$  as a function of  $M_{UV}$  by the abundance matching method with and without DC and HOD terms, using

$$\begin{aligned} & \int_0^\infty dM'_h \frac{dn}{dM'_h}(M'_h, z) \times DC \times HOD(M'_h, M_h) \\ &= \int_{M_{UV}}^{-\infty} dM'_{UV} \Phi(M'_{UV}, z), \end{aligned} \quad (65)$$

where  $\frac{dn}{dM'_h}(M'_h, z)$  and  $\Phi(M'_{UV}, z)$  are the halo mass function and the UV luminosity function at  $z \sim 4$ , respectively. The term of  $HOD(M'_h, M_h)$  is changed on a case-by-case basis, as detailed below.

The calculation results are shown in the  $M_h$  vs.  $M_{UV}$  plot of Figure 13. The black solid curve represents the SiAM case that includes neither DC nor HOD effect, i.e.,  $DC = 1$  and  $HOD(M'_h, M_h) = H(M'_h - M_h)$ , where  $H(x)$  is a step function. The red dashed curve corresponds to the no-HOD case with the DC effects,  $DC = 0.6$  and  $HOD(M'_h, M_h) = H(M'_h - M_h)$ . The red dot-dashed curve denotes the no-DC case with the HOD effects,  $DC = 1.0$  and  $HOD(M'_h, M_h) = N_c(M'_h) + N_s(M'_h)$ , where we use our best-fit HOD parameter set of the  $z \sim 4$  LBG subsample of  $m_{UV} < 28.2$  mag that is well determined,  $(\sigma_{\log M}, \log M_0, \log M'_1, \alpha) = (0.2, 11.5, 12.1, 1.0)$ , and  $M_{\min} = M_h$  by definition. The red solid curve indicates the best-estimate case with the DC and HOD effects, mimicking our clustering analysis results,  $DC = 0.6$  and  $HOD(M'_h, M_h) = N_c(M'_h) + N_s(M'_h)$ .

Comparing the best-estimate case with the DC and HOD effects (red solid curve) in Figure 13, we find that the no-DC case (red dot-dashed curve) overestimates  $M_h$  by  $\sim 0.2$  dex at the faint magnitude of  $M_{UV} \sim -16$  mag. However, this overestimate becomes small at the bright magnitude, suggesting that the DC effect is more important at the faint magnitude. In contrast to the no-DC case, the no-HOD case (red dashed curve) agrees with the best-estimate case (red solid curve) at the faint mag-

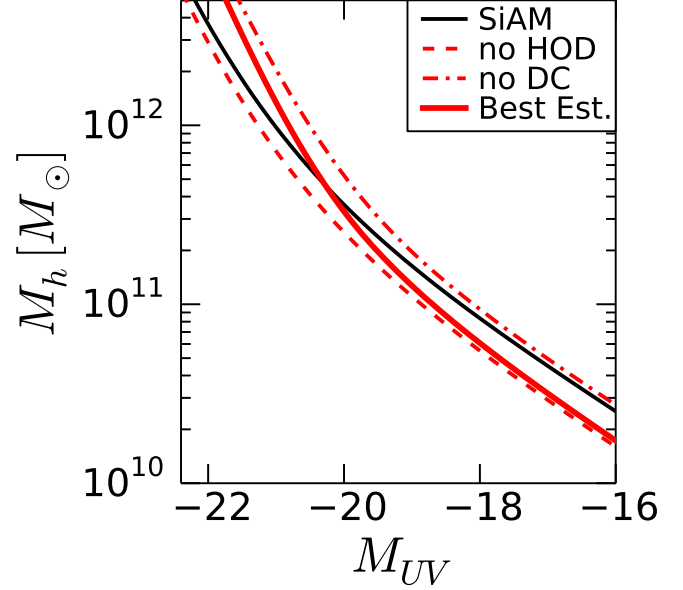


**Figure 13.** Impact of DC and HOD on the dark matter halo mass estimates. We plot the dark matter halo mass estimates for our  $z \sim 4$  subsample as a function of absolute magnitude. The black curve is the result of the simple abundance matching (SiAM). The dashed curve represents the result of the abundance matching with  $DC = 0.6$ . The dot-dashed curve denotes the result of the abundance matching considering the HOD ( $\sigma_{\log M} = 0.2$ ,  $\log M_0 = 11.5$ ,  $\log M'_1 = 12.1$ , and  $\alpha = 1.0$ ) with  $DC = 1.0$ . The red solid curve is the result of the abundance matching considering the HOD with  $DC = 0.6$ , mimicking our clustering analysis results. See Section 7.3.1 for more details.

nitude, while the no-HOD case underestimates  $M_h$  by 0.4 dex at the bright magnitude of  $M_{UV} = -21.5$  mag. Note that the SiAM case (black solid curve) is bracketed by the no-DC case (red dot-dashed curve) and the no-HOD case (red dashed curve). The SiAM case overestimates (underestimates)  $M_h$  at the faint (bright) magnitudes by  $\sim 0.2$  ( $\sim 0.4$ ) dex, following the no-DC (no-HOD) case. Because the DC and HOD effects cancel out, the SiAM case provides  $M_h$  values comparable to those of the best-estimate case at the intermediate magnitude of  $M_{UV} \sim -21$  ( $-20$ ) mag that corresponds to  $L^*$ .

#### 7.3.2. Comparisons with the Abundance Matching Results

We compare results of our clustering analyses with those of recent abundance matching studies. Figure 14 presents halo masses estimated by abundance matching techniques of Behroozi et al. (2013a) and Moster et al. (2013), together with our halo mass estimates from the clustering analyses. Here, again, we use the modified results of Behroozi et al. (2013a) whose cosmological parameters and stellar-mass estimate assumptions are the same as ours (P. Behroozi in private communication). Figure 15 (Figure 16) is the same as Figure 14, but for Finkelstein et al. (2015), Trac et al. (2015), and Mason et al. (2015) (Mashian et al. 2015). Although the comparisons in the  $M_h$  vs.  $M_*$  or  $SHMR$  vs.  $M_h$  plot (Figure 14) are straightforward, we use  $M_h$  vs.  $M_{UV}$  and  $M_h$  vs. SFR in Figures 15 and 16, respectively. This is because the abundance matching studies shown in Figures 15 and 16 do not present  $M_*$ , but  $M_{UV}$  or SFR.

In Figure 14, we find that the abundance matching re-

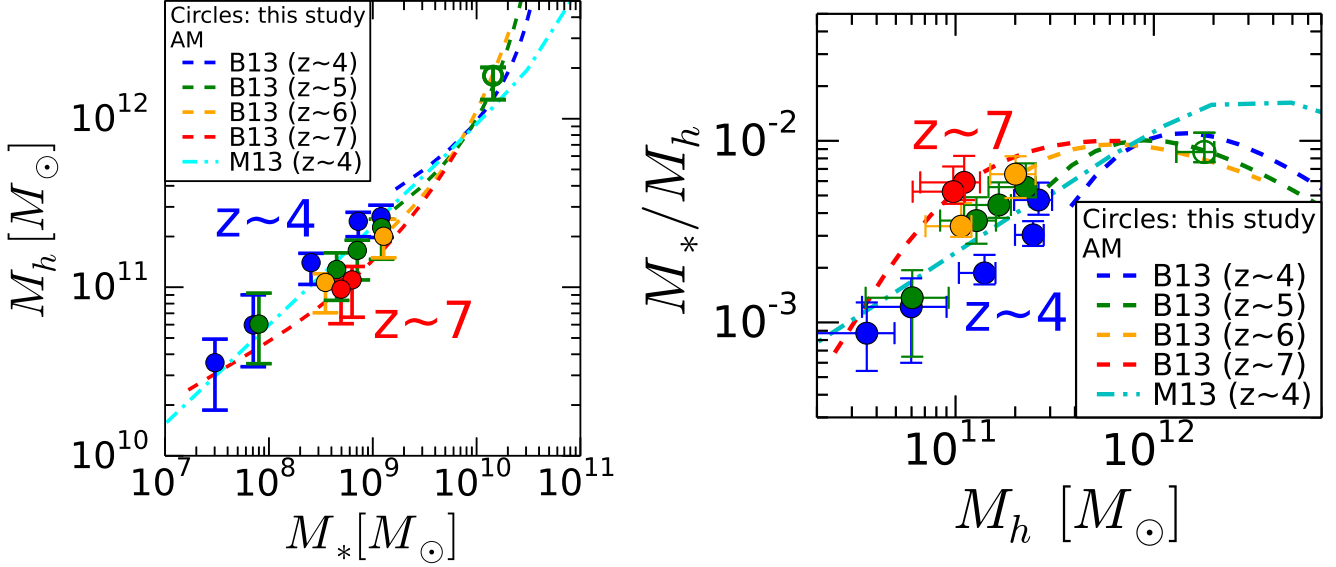


**Figure 14.** Comparison with Behroozi et al. (2013a) and Moster et al. (2013). Left panel: comparison of the dark matter halo mass as a function of stellar mass. The blue, green, orange, and red dashed curves are the results of Behroozi et al. (2013a). The cyan dot-dashed curve is the result of Moster et al. (2013). The blue, green, orange, and red circles represent the dark matter halo mass of our Hubble subsamples at  $z \sim 4, 5, 6$ , and  $7$ , respectively. The open green circle denotes the dark matter halo mass of our subsample constructed from the HSC data. Right panel: comparison of the SHMR. Same as the left panel but the horizontal and vertical axes are the dark matter halo mass and the SHMR.

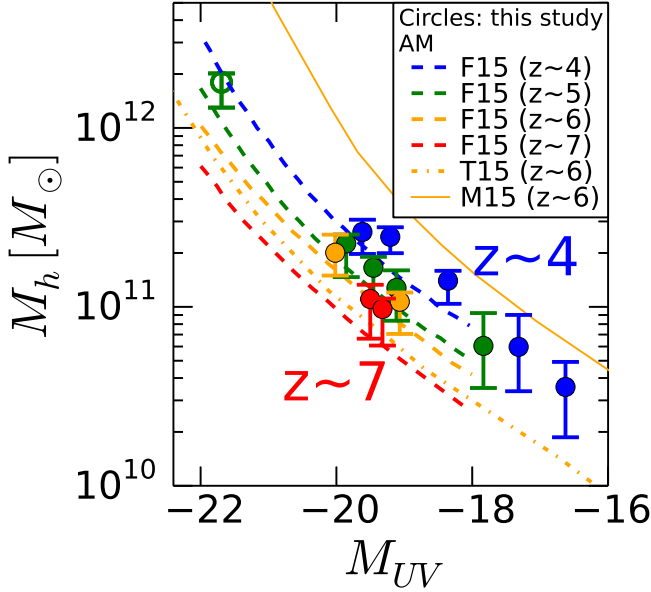


**Figure 15.** Comparison with Finkelstein et al. (2015), Trac et al. (2015) and Mason et al. (2015). The blue, green, orange, and red dashed curves are the results of Finkelstein et al. (2015) at  $z \sim 4, 5, 6$ , and  $7$ , respectively. The orange dot-dashed and the solid curve shows the  $z \sim 6$  results of Trac et al. (2015) and Mason et al. (2015), respectively. The blue, green, orange, and red circles represent the dark matter halo masses of our subsamples at  $z \sim 4, 5, 6$ , and  $7$ , respectively.

sults of Behroozi et al. (2013a) agree with our clustering results at  $z \sim 5 - 7$  very well within  $1\sigma$  errors. At  $z \sim 4$ , the stellar mass range of Behroozi et al. (2013a) does not cover the one of ours, and secure comparisons cannot be made.

Figure 15 indicates that the abundance matching re-

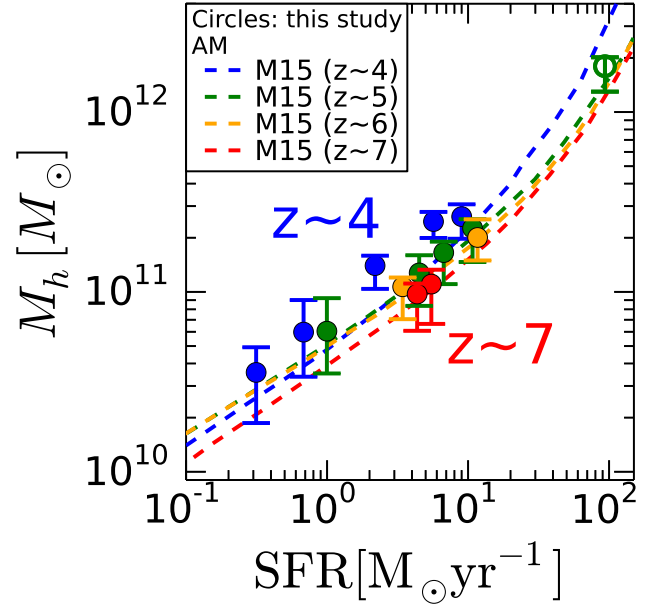


**Figure 16.** Comparison with Mashian et al. (2015). The blue, green, orange, and red dashed curves are the results of Mashian et al. (2015) at  $z \sim 4, 5, 6$ , and  $7$ , respectively. The blue, green, orange, and red circles represent the dark matter halo masses of our subsamples at  $z \sim 4, 5, 6$ , and  $7$ , respectively.

sults in Finkelstein et al. (2015) are consistent with our clustering results within  $1\sigma$  errors at  $z \sim 5 - 7$ , although all of the data of Finkelstein et al. (2015) appear to fall below our clustering results. At  $z \sim 4$ , the  $M_h$  values of Finkelstein et al. (2015) are lower than ours by 0.13 dex at  $z \sim 4$  at the  $\sim 2\sigma$  levels. There are similar  $\sim 2\sigma$  level  $M_h$  value offsets of 0.1 ( $\sim 0.2$ ) dex to

Moster et al. (2013) (Trac et al. 2015 and Mashian et al. 2015) at  $z \sim 4$  ( $z \sim 6$  and 4). Note that all of these studies adopt the cosmological parameters different from ours. The cosmological parameter sets used in Moster et al. (2013), Trac et al. (2015), and Mashian et al. (2015) are  $(H_0, \Omega_m, \Omega_\Lambda, \sigma_8) = (70.4, 0.272, 0.728, 0.810)$ ,  $(70, 0.27, 0.73, 0.8)$ , and  $(70, 0.3, 0.7, 0.82)$ , respectively. Finkelstein et al. (2015) use the parameter sets of  $(H_0, \Omega_m, \Omega_\Lambda) = (70.2, 0.275, 0.725)$ . If we correct these study results for the effects of the different cosmological parameters, the duty cycle, and the halo mass function, these study results agree with our clustering analysis estimates within  $\sim 0.1$  dex. In other words, all of these abundance matching results agree with our clustering results very well. In Section 7.3.1, we compare the results of SiAM with those of the best estimates having clustering analysis parameter constraints, and conclude that the SiAM results differ from the best estimates up to 0.4 dex in  $M_h$ . However, we find very good agreements between the recent abundance matching studies and the clustering analysis study, within  $\sim 0.1$  dex in  $M_h$ . These good agreements are probably explained by the facts that these abundance matching studies are different from the classical technique of SiAM, but with the subhalos, incompleteness (similar to DC; Behroozi et al. 2013a), and/or SFR+stellar mass function evolution that reduce the systematics.

In Figure 15, we find that the dark matter halo masses of Mason et al. (2015) are larger than ours by 0.8 dex at the  $> 5\sigma$  levels. These large differences probably originate from the assumption in Mason et al. (2015) that the SHMR does not evolve from  $z \sim 5$ .

### 7.3.3. Conclusions of the Comparisons

In Section 7.3.2, we find that  $M_h$  estimates from our clustering analyses agree with most of the abundance matching results within the  $\sim 0.1$  dex level at  $z \sim 4 - 7$ , which are corrected for the differences of cosmological parameters, the duty cycle values, and the halo mass functions. Although there exist the systematic  $M_h$  differences originating from the DC and HOD uncertainties up to by 0.4 dex or a factor of 3 in the SiAM at the dark matter halo mass of  $10^{10} - 10^{12} M_\odot$  (Section 7.3.1), the recent abundance matching techniques including the subhalos, incompleteness, and/or SFR+stellar-mass evolution, appear to reduce the systematics down to the  $\sim 0.1$  dex level. Thus, the abundance matching techniques are useful to estimate  $M_h$  of high- $z$  galaxy halos, if one allows the systematic uncertainties up to a factor of 3. The good agreements between the clustering and abundance matching techniques are found, probably because the systematics of the subhalo-galaxy relation is small due to the small satellite fraction at high- $z$  (Zheng et al. 2007; Coupon et al. 2012; see also Jaacks et al. 2015).

## 8. SUMMARY

We obtain clustering measurements of  $z \sim 4 - 7$  galaxies from the data set of the legacy deep Hubble/ACS and WFC3 images and the complimentary large-area Subaru/HSC images that are newly available. Via our HOD modeling, we investigate SHMRs at  $z \sim 4 - 7$  for the first time by galaxy clustering analyses. We compare our clustering analysis results with the abundance matching

results that are actively being obtained by recent studies. Our major findings are summarized below.

1. The mean dark matter halo masses of our LBGs at  $z \sim 4 - 7$  are  $\langle M_h \rangle \sim (1 - 20) \times 10^{11} M_\odot$ . There is an increasing trend in the dark matter halo mass with increasing the UV luminosity of LBGs at  $z \sim 4 - 7$ . Our estimated dark matter halo masses are consistent with the previous clustering studies in the  $\langle M_h \rangle - \langle M_{UV} \rangle$  plane, if we use the same cosmological parameter set for comparison.
2. We estimate SHMR, that is the stellar-to-halo mass ratio, for our LBGs. We identify the SHMR evolutions in  $z \sim 0 - 4$  and  $z \sim 4 - 7$  at the  $> 98\%$  confidence level for the first time based on clustering analyses. We find that, at the dark matter halo mass of  $M_h \sim 10^{11} M_\odot$ , SHMRs decrease by a factor of  $\sim 3$ , from  $\sim 3 \times 10^{-3}$  ( $z \sim 0$ ) to  $\sim 1 \times 10^{-3}$  ( $z \sim 4$ ), and increase by a factor of  $\sim 5$ , from  $\sim 1 \times 10^{-3}$  ( $z \sim 4$ ) to  $\sim 5 \times 10^{-3}$  ( $z \sim 7$ ).
3. We calculate BCE, that is the ratio of the SFR to the baryon accretion rate corresponding to rates of the conversion from gas to stars. The BCEs at  $z \sim 4$  increase from  $\sim 3 \times 10^{-2}$  to  $\sim 1 \times 10^{-1}$  with increasing dark matter halo mass up to  $\sim 10^{12} M_\odot$ . The low mass halos form stars inefficiently, probably due to feedback effects and/or slow gas cooling.
4. We compare our clustering+HOD results with abundance matching estimates. We find that the  $M_h$  estimates of clustering+HOD analyses agree with those of the simple abundance matching within a factor of 3. Moreover, the results of the recent studies' sophisticated abundance matching techniques including the subhalos, incompleteness, and/or SFR+stellar-mass evolution are even better than those of the simple abundance matching technique, some of which agree with our clustering results within 0.1 dex at  $z \sim 4 - 7$ . Due to the small galaxy occupation in one-halo at high- $z$ , abundance matching techniques are useful to estimate  $M_h$  for high- $z$  galaxies, if one allows these reasonably small uncertainties raised by the assumptions of the abundance matching techniques.

We are grateful to Peter Behroozi for useful discussions and providing his SHMR results that are recalculated with the cosmological parameters and stellar mass estimates same as ours. We appreciate helpful comments on an early draft version of this paper from Michael A. Strauss and Masahiro Takada. We thank Jim Bosch, Hisanori Furusawa, Robert H. Lupton, Sogo Mineo, and Naoki Yasuda for their helpful comments and discussions on the treatment of the HSC data. We are also grateful to Masayuki Tanaka for kindly providing a masking code and discussing our results. This work has benefited from many interesting conversations with Renyue Cen, Motohiro Enoki, Ryosuke Goto, Masao Hayashi, Chiaki Hikage, Yutaka Hirai, Soh Ikarashi, Akio Inoue, Masaru Kajisawa, Nobunari Kashikawa, Daichi Kashino, Masakazu A.R.

Kobayashi, Masato I.N. Kobayashi, Andrei Mesinger, Kentaro Nagamine, Tohru Nagao, Masahiro Nagashima, Atsushi J. Nishizawa, Takashi Okamoto, Kouji Ohta, Taku Okamura, Jaehong Park, Tsutomu Takeuchi, and Masayuki Umemura.

This work is based on observations taken by the 3D-HST Treasury Program (GO 12177 and 12328) and CANDELS Multi-Cycle Treasury Program with the NASA/ESA HST, which is operated by the Association of Universities for Research in Astronomy, Inc., under NASA contract NAS5-26555. This paper makes use of software developed for the Large Synoptic Survey Telescope. We thank the LSST Project for making their code available as free software at <http://dm.lsstcorp.org>.

The Pan-STARRS1 Surveys (PS1) have been made possible through contributions of the Institute for Astronomy, the University of Hawaii, the Pan-STARRS Project Office, the Max-Planck Society and its participating institutes, the Max Planck Institute for Astronomy, Heidelberg and the Max Planck Institute for Extraterrestrial Physics, Garching, The Johns Hopkins University, Durham University, the University of Edinburgh, Queen's University Belfast, the Harvard-Smithsonian Center for Astrophysics, the Las Cumbres Observatory Global Telescope Network Incorporated, the National Central University of Taiwan, the Space Telescope Science Institute, the National Aeronautics and Space Administration under Grant No. NNX08AR22G issued through the Planetary Science Division of the NASA Science Mission Directorate, the National Science Foundation under Grant No. AST-1238877, the University of Maryland, and Eotvos Lorand University (ELTE).

This work is supported by World Premier International Research Center Initiative (WPI Initiative), MEXT, Japan, and KAKENHI (23244025) and (15H02064) Grant-in-Aid for Scientific Research (A) through Japan Society for the Promotion of Science (JSPS). Y.H. is supported by an Advanced Leading Graduate Course for Photon Science grant (ALPS). S.M. is supported by KAKENHI (15K17600).

*Facilities:* HST (ACS, WFC3), Subaru (HSC, Suprime-Cam), CFHT (MEGACAM).

## REFERENCES

- Alam, S., Albareti, F. D., Allende Prieto, C., et al. 2015, *ApJS*, 219, 12
- Axelrod, T., Kantor, J., Lupton, R. H., & Pierfederici, F. 2010, in *Society of Photo-Optical Instrumentation Engineers (SPIE) Conference Series*, Vol. 7740, Society of Photo-Optical Instrumentation Engineers (SPIE) Conference Series, 15
- Barone-Nugent, R. L., Trenti, M., Wyithe, J. S. B., et al. 2014, *ApJ*, 793, 17
- Bartelmann, M., & Schneider, P. 2001, *Phys. Rep.*, 340, 291
- Beckwith, S. V. W., Stiavelli, M., Koekemoer, A. M., et al. 2006, *AJ*, 132, 1729
- Behroozi, P. S., Wechsler, R. H., & Conroy, C. 2013a, *ApJ*, 770, 57
- Behroozi, P. S., Wechsler, R. H., & Wu, H.-Y. 2013b, *ApJ*, 762, 109
- Berlind, A. A., & Weinberg, D. H. 2002, *ApJ*, 575, 587
- Berlind, A. A., Weinberg, D. H., Benson, A. J., et al. 2003, *ApJ*, 593, 1
- Bertin, E., & Arnouts, S. 1996, *A&AS*, 117, 393
- Bertin, E., Mellier, Y., Radovich, M., et al. 2002, in *Astronomical Society of the Pacific Conference Series*, Vol. 281, *Astronomical Data Analysis Software and Systems XI*, ed. D. A. Bohlender, D. Durand, & T. H. Handley, 228
- Birrer, S., Lilly, S., Amara, A., Paranjape, A., & Refregier, A. 2014, *ApJ*, 793, 12
- Bouwens, R. J., Illingworth, G. D., Oesch, P. A., et al. 2010, *ApJ*, 708, L69
- . 2011, *ApJ*, 737, 90
- . 2015, *ApJ*, 803, 34
- Brammer, G. B., van Dokkum, P. G., Franx, M., et al. 2012, *ApJS*, 200, 13
- Bruzual, G., & Charlot, S. 2003, *MNRAS*, 344, 1000
- Bullock, J. S., Kolatt, T. S., Sigad, Y., et al. 2001, *MNRAS*, 321, 559
- Chabrier, G. 2003, *PASP*, 115, 763
- Conroy, C., Wechsler, R. H., & Kravtsov, A. V. 2006, *ApJ*, 647, 201
- Cooray, A., & Sheth, R. 2002, *Phys. Rep.*, 372, 1
- Coupon, J., Kilbinger, M., McCracken, H. J., et al. 2012, *A&A*, 542, A5
- Coupon, J., Arnouts, S., van Waerbeke, L., et al. 2015, *MNRAS*, 449, 1352
- Daddi, E., Dickinson, M., Morrison, G., et al. 2007, *ApJ*, 670, 156
- Dekel, A., Birnboim, Y., Engel, G., et al. 2009, *Nature*, 457, 451
- Durkalec, A., Le Fèvre, O., de la Torre, S., et al. 2015, *A&A*, 576, L7
- Efstathiou, G., Bernstein, G., Tyson, J. A., Katz, N., & Guhathakurta, P. 1991, *ApJ*, 380, L47
- Ellis, R. S., McLure, R. J., Dunlop, J. S., et al. 2013, *ApJ*, 763, L7
- Erb, D. K., Steidel, C. C., Shapley, A. E., et al. 2006, *ApJ*, 646, 107
- Fakhouri, O., Ma, C.-P., & Boylan-Kolchin, M. 2010, *MNRAS*, 406, 2267
- Finkelstein, S. L., Song, M., Behroozi, P., et al. 2015, *ArXiv e-prints*, arXiv:1504.00005
- Fisher, K. B., Davis, M., Strauss, M. A., Yahil, A., & Huchra, J. P. 1994, *MNRAS*, 267, 927
- Foucaud, S., Conselice, C. J., Hartley, W. G., et al. 2010, *MNRAS*, 406, 147
- Foucaud, S., McCracken, H. J., Le Fèvre, O., et al. 2003, *A&A*, 409, 835
- Garel, T., Blaizot, J., Guiderdoni, B., et al. 2015, *MNRAS*, 450, 1279
- Grogin, N. A., Kocevski, D. D., Faber, S. M., et al. 2011, *ApJS*, 197, 35
- Groth, E. J., & Peebles, P. J. E. 1977, *ApJ*, 217, 385
- Guo, H., Zheng, Z., Behroozi, P. S., et al. 2015, *ArXiv e-prints*, arXiv:1508.07012
- Hamana, T., Ouchi, M., Shimasaku, K., Kayo, I., & Suto, Y. 2004, *MNRAS*, 347, 813
- Harikane, Y., Ouchi, M., Yuma, S., et al. 2014, *ApJ*, 794, 129
- Hatfield, P. W., Lindsay, S. N., Jarvis, M. J., et al. 2015, *ArXiv e-prints*, arXiv:1511.05476
- Hildebrandt, H., Pielorz, J., Erben, T., et al. 2009, *A&A*, 498, 725
- Hudson, M. J., Gillis, B. R., Coupon, J., et al. 2015, *MNRAS*, 447, 298
- Illingworth, G. D., Magee, D., Oesch, P. A., et al. 2013, *ApJS*, 209, 6
- Ishigaki, M., Kawamata, R., Ouchi, M., et al. 2015, *ApJ*, 799, 12
- Ivezic, Z., Tyson, J. A., Abel, B., et al. 2008, *ArXiv e-prints*, arXiv:0805.2366
- Jaacks, J., Finkelstein, S. L., & Nagamine, K. 2015, *ArXiv e-prints*, arXiv:1507.00713
- Jee, M. J., & Tyson, J. A. 2011, *PASP*, 123, 596
- Kawamata, R., Ishigaki, M., Shimasaku, K., Oguri, M., & Ouchi, M. 2015, *ApJ*, 804, 103
- Kereš, D., Katz, N., Davé, R., Fardal, M., & Weinberg, D. H. 2009, *MNRAS*, 396, 2332
- Koekemoer, A. M., Faber, S. M., Ferguson, H. C., et al. 2011, *ApJS*, 197, 36
- Koekemoer, A. M., Ellis, R. S., McLure, R. J., et al. 2013, *ApJS*, 209, 3
- Kravtsov, A. V., Berlind, A. A., Wechsler, R. H., et al. 2004, *ApJ*, 609, 35
- Landy, S. D., & Szalay, A. S. 1993, *ApJ*, 412, 64
- Leauthaud, A., Tinker, J., Behroozi, P. S., Busha, M. T., & Wechsler, R. H. 2011, *ApJ*, 738, 45
- Leauthaud, A., Tinker, J., Bundy, K., et al. 2012, *ApJ*, 744, 159
- Lee, K.-S., Giavalisco, M., Conroy, C., et al. 2009, *ApJ*, 695, 368
- Lee, K.-S., Giavalisco, M., Gnedin, O. Y., et al. 2006, *ApJ*, 642, 63

- Ling, E. N., Barrow, J. D., & Frenk, C. S. 1986, *MNRAS*, 223, 21P
- Magnier, E. A., Schlafly, E., Finkbeiner, D., et al. 2013, *ApJS*, 205, 20
- Mandelbaum, R., Seljak, U., Kauffmann, G., Hirata, C. M., & Brinkmann, J. 2006, *MNRAS*, 368, 715
- Martinez-Manso, J., Gonzalez, A. H., Ashby, M. L. N., et al. 2015, *MNRAS*, 446, 169
- Mashian, N., Oesch, P., & Loeb, A. 2015, *ArXiv e-prints*, arXiv:1507.00999
- Mason, C., Trenti, M., & Treu, T. 2015, *ArXiv e-prints*, arXiv:1508.01204
- McBride, C., Berlind, A., Scoccimarro, R., et al. 2009, in *Bulletin of the American Astronomical Society*, Vol. 41, American Astronomical Society Meeting Abstracts #213, 253
- McCracken, H. J., Wolk, M., Colombi, S., et al. 2015, *MNRAS*, 449, 901
- Mitchell, P., Lacey, C., Baugh, C., & Cole, S. 2015, *ArXiv e-prints*, arXiv:1510.08463
- Miyazaki, S., Komiyama, Y., Nakaya, H., et al. 2012, in *Society of Photo-Optical Instrumentation Engineers (SPIE) Conference Series*, Vol. 8446, Society of Photo-Optical Instrumentation Engineers (SPIE) Conference Series, 0
- Mo, H. J., Jing, Y. P., & Boerner, G. 1992, *ApJ*, 392, 452
- More, S., Miyatake, H., Mandelbaum, R., et al. 2015, *ApJ*, 806, 2
- More, S., van den Bosch, F. C., Cacciato, M., et al. 2011, *MNRAS*, 410, 210
- Moster, B. P., Naab, T., & White, S. D. M. 2013, *MNRAS*, 428, 3121
- Murray, N., Quataert, E., & Thompson, T. A. 2005, *ApJ*, 618, 569
- Navarro, J. F., Frenk, C. S., & White, S. D. M. 1996, *ApJ*, 462, 563
- . 1997, *ApJ*, 490, 493
- Okamoto, T., Shimizu, I., & Yoshida, N. 2014, *PASJ*, 66, 70
- Ouchi, M., Shimasaku, K., Okamura, S., et al. 2001, *ApJ*, 558, L83
- . 2004a, *ApJ*, 611, 660
- . 2004b, *ApJ*, 611, 685
- Ouchi, M., Hamana, T., Shimasaku, K., et al. 2005, *ApJ*, 635, L117
- Ouchi, M., Shimasaku, K., Furusawa, H., et al. 2010, *ApJ*, 723, 869
- Park, J., Kim, H.-S., Wyithe, J. S. B., et al. 2015, *ArXiv e-prints*, arXiv:1511.01983
- Peebles, P. J. E. 1980, *The large-scale structure of the universe* (Princeton University Press)
- Reddick, R. M., Wechsler, R. H., Tinker, J. L., & Behroozi, P. S. 2013, *ApJ*, 771, 30
- Roche, N., & Eales, S. A. 1999, *MNRAS*, 307, 703
- Rodríguez-Puebla, A., Avila-Reese, V., Yang, X., et al. 2015, *ApJ*, 799, 130
- Saito, S., Leauthaud, A., Hearin, A. P., et al. 2015, *ArXiv e-prints*, arXiv:1509.00482
- Salpeter, E. E. 1955, *ApJ*, 121, 161
- Schlafly, E. F., Finkbeiner, D. P., Jurić, M., et al. 2012, *ApJ*, 756, 158
- Scoville, N., Sheth, K., Aussel, H., et al. 2015, *ArXiv e-prints*, arXiv:1505.02159
- Seljak, U. 2000, *MNRAS*, 318, 203
- Shan, H., Kneib, J.-P., Li, R., et al. 2015, *ArXiv e-prints*, arXiv:1502.00313
- Shibuya, T., Ouchi, M., & Harikane, Y. 2015, *ArXiv e-prints*, arXiv:1503.07481
- Shimizu, M., Kitayama, T., Sasaki, S., & Suto, Y. 2003, *ApJ*, 590, 197
- Silk, J., & Wyse, R. F. G. 1993, *Phys. Rep.*, 231, 293
- Skelton, R. E., Whitaker, K. E., Momcheva, I. G., et al. 2014, *ApJS*, 214, 24
- Skibba, R. A., Coil, A. L., Mendez, A. J., et al. 2015, *ApJ*, 807, 152
- Somerville, R. S., Lee, K., Ferguson, H. C., et al. 2004, *ApJ*, 600, L171
- Song, M., Finkelstein, S. L., Ashby, M. L. N., et al. 2015, *ArXiv e-prints*, arXiv:1507.05636
- Steidel, C. C., Adelberger, K. L., Giavalisco, M., Dickinson, M., & Pettini, M. 1999, *ApJ*, 519, 1
- Tinker, J., Kravtsov, A. V., Klypin, A., et al. 2008, *ApJ*, 688, 709
- Tinker, J. L., Robertson, B. E., Kravtsov, A. V., et al. 2010, *ApJ*, 724, 878
- Tonry, J. L., Stubbs, C. W., Lykke, K. R., et al. 2012, *ApJ*, 750, 99
- Trac, H., Cen, R., & Mansfield, P. 2015, *ArXiv e-prints*, arXiv:1507.02685
- van den Bosch, F. C., More, S., Cacciato, M., Mo, H., & Yang, X. 2013, *MNRAS*, 430, 725
- Whitaker, K. E., Franx, M., Leja, J., et al. 2014, *ApJ*, 795, 104
- Yagi, M., Kashikawa, N., Sekiguchi, M., et al. 2002, *AJ*, 123, 66
- Zehavi, I., Zheng, Z., Weinberg, D. H., et al. 2005, *ApJ*, 630, 1
- Zheng, Z., Coil, A. L., & Zehavi, I. 2007, *ApJ*, 667, 760
- Zheng, Z., Berlind, A. A., Weinberg, D. H., et al. 2005, *ApJ*, 633, 791